JOURNAL OF GUIDANCE, CONTROL, AND DYNAMICS
Vol. 49, No. 4, April 2026

Cislunar Mean-Motion Resonances: Definitions, Widths, and Comparisons with Resonant Satellites

Anjali Rawat*
Virginia Polytechnic Institute and State University, Blacksburg, Virginia 24061
Bhanu Kumar†
University of Michigan, Ann Arbor, Michigan 48109
Aaron J. Rosengren‡
University of California, San Diego, La Jolla, California 92093
and
Shane D. Ross§
Virginia Polytechnic Institute and State University, Blacksburg, Virginia 24061

https://doi.org/10.2514/1.G009336

Lunar mean-motion resonances (MMRs) significantly shape cislunar dynamics beyond geosynchronous orbit, forming stable/unstable orbit pairs with corresponding intermingled chaotic and regular regions. The resonance zone is rigorously defined using the separatrices of unstable resonant periodic orbits surrounding stable quasi-periodic regions. Our study leverages the planar circular restricted three-body problem to estimate the (stable) resonance widths and (unstable) chaotic resonance zones of influence of the 2:1 and 3:1 MMRs across various Jacobi constants, employing a Poincaré map at perigee and presenting findings in easily interpretable geocentric orbital elements. An analysis of the semi-major axis versus eccentricity plane reveals broader regions of resonance influence than those predicted by semi-analytical models based on the perturbed Kepler problem. A comparison with high-fidelity three-dimensional ephemeris propagation of several spacecraft (TESS, IBEX, and Spektr-R) in these regions is made, which shows good agreement with the simplified circular restricted three-body problem model.

Nomenclature

a	=	semi-major axis, nondimensional distance unit
C	=	Jacobi constant
e	=	eccentricity
$\mathcal{G}$	=	gravitational constant, $\mathrm{km}^3/(\mathrm{kg}\cdot\mathrm{s}^2)$
H, h, G, g, L, ℓ	=	Delaunay variables
i	=	inclination with respect to the Moon's orbital plane, rad
k	=	number of geocentric orbits completed by spacecraft in Earth-centered inertial frame
ℓ	=	mean anomaly, rad
m_e, m_m	=	mass of Earth, Moon, kg
m_1, m_2	=	mass of primary, secondary
n_m	=	Moon's mean motion, s^{-1}
$R^{\mathrm{eclip}}_{\mathrm{eci}}$	=	rotation matrix to convert from geocentric equatorial to ecliptic frame
$R^{\mathrm{syn}}_{\mathrm{iner}}$	=	rotation matrix to convert from geocentric inertial ecliptic to synodic frame
$\boldsymbol{r}$, $\boldsymbol{v}$	=	position (km) and velocity (km/s) vectors of spacecraft in Earth-centered inertial frame
r_1, r_2	=	distance from spacecraft to primary, secondary, nondimensional distance unit
T	=	inertial-frame period of spacecraft, nondimensional time unit
$\boldsymbol{v}_{m,\mathrm{cir}}$	=	velocity of the Moon under circular motion assumption, km/s
$\hat{\boldsymbol{x}}$, $\hat{\boldsymbol{y}}$, $\hat{\boldsymbol{z}}$	=	instantaneous unit vectors for synodic frame
$\dot{\hat{\boldsymbol{x}}}$, $\dot{\hat{\boldsymbol{y}}}$, $\dot{\hat{\boldsymbol{z}}}$	=	instantaneous rate of change of unit vectors for synodic frame
ε	=	obliquity of the ecliptic, rad
λ	=	spacecraft's mean longitude, rad
μ	=	mass ratio of Earth–Moon system
μ_e, μ_m	=	gravitational parameter of Earth $\mathcal{G}m_e$, Moon $\mathcal{G}m_m$, $\mathrm{km}^3/\mathrm{s}^2$
ν	=	true anomaly, rad
Ω	=	longitude of ascending node in synodic frame, rad
ω	=	argument of perigee, rad
ϖ	=	longitude of perigee in synodic frame, rad
ω_m	=	angular velocity of Moon, rad/s

Subscripts

e	=	Earth
iner	=	inertial frame
m	=	Moon
non-dim	=	nondimensionalized
syn	=	synodic frame

I. Introduction

THE dynamics of cislunar space beyond geosynchronous orbit (xGEO) are fundamentally influenced by mean-motion resonances (MMRs), a phenomenon previously underappreciated in Earth–satellite dynamics due to their negligible effect on the traditional geocentric domains. However, for missions like IBEX and TESS, which operate within predominant lunar MMRs, and others like Spektr-R, which seemingly navigates unstable resonance regions, recognizing the impact of MMRs is crucial. Determining

Presented as Paper 24-368 at the AAS/AIAA Astrodynamics Specialist Conference, Broomfield, CO, August 11–15, 2024; received 12 May 2025; accepted for publication 18 October 2025; published online 24 December 2025.

*Ph.D. Student, Aerospace and Ocean Engineering; anjalirawat@vt.edu.
†James Van Loo Postdoctoral Assistant Professor, Department of Mathematics; also NSF Postdoctoral Research Fellow, Jet Propulsion Laboratory, California Institute of Technology, Pasadena, California 91109; bhkumar@umich.edu.
‡Assistant Professor, Mechanical and Aerospace Engineering; arosengren@ucsd.edu.
§Professor, Aerospace and Ocean Engineering; sdross@vt.edu.

the stability of a space asset's xGEO orbit necessitates a thorough understanding of the dynamical structure of MMRs, particularly the extent of stable MMRs and the surrounding chaotic regions across various semi-major axis values.

Semi-analytical methods, such as Gallardo's algorithm [1], have been used to assess the domains of influence of predominant MMRs in planetary dynamics. Yet, these methods often presuppose constant eccentricity over resonant time scales, which does not reflect the highly perturbed Earth–Moon environment of xGEO. Such approaches, moreover, are fundamentally based on the perturbed-Hamiltonian formulation, which yields a local, rather than global, description of phase space; they consequently underestimate the true regions of influence of MMRs. A global geometric dynamical portrait can be furnished by semi-analytical approaches to the circular restricted three-body problem (CR3BP). Although some methods incorporate the CR3BP model, they rely on narrowly defined initial conditions that generate localized Poincaré maps specific to a given resonance [2], thus overlooking the intricate global dynamics of phase space. Typically, a Poincaré map at $y = 0$ is employed [3], but it provides limited insight into the dynamical structure of resonant orbits. Although Ref. [4] employs a Poincaré map at perigee to determine the precise widths of interior first-order resonances in the Sun–Jupiter system, their analysis does not include visualizations of these maps in orbital elements, which offer more interpretability. Additionally, these studies tend to neglect the presence of unstable resonant periodic orbits. Although Refs. [5–7] demonstrate usage of manifolds of unstable resonant orbits for natural transport, they focus on specific orbits. Global quantification of chaotic resonance zones is entirely neglected, even though they are essential for understanding transit across the extensive connected chaotic regions that prevail over a broad span of Jacobi constant values.

This study computes the semi-major axis *stable resonance widths* and the larger circumscribing *unstable resonance zones* of influence for key lunar MMRs, specifically the 2:1 and 3:1 resonances, using the planar (P)CR3BP and following known methods for its study [8–12]. By applying a Poincaré map at the perigee of osculating orbits [10,12], we delineate these regions in the plane of semi-major axis and *synodic* longitude of perigee ϖ (the longitude of perigee relative to the Earth–Moon line). Our Poincaré maps reveal resonance regions, notably the prominent 2:1, 3:1, and 4:1 resonance *islands*, through which we can determine the *stable* width of a resonance, defined as the semi-major axis span of the *largest* (i.e., outermost) stable quasi-periodic torus. According to the Poincaré–Birkhoff theorem [13,14], stable resonant points (the centers of the islands) will alternate with unstable resonant points, which will be embedded in a (perhaps large) chaotic set. These unstable resonant periodic orbits can be computed via symmetry, and their stable and unstable manifolds calculated and visualized on the same Poincaré map. Chaotic (resonance) zones are identified as regions enclosed by segments of stable and unstable manifolds that form the regions' boundaries, according to well-established dynamical-systems methods [15,16]. Resonance widths and the larger enclosing chaotic resonance zones are computed across a range of Jacobi constants, subsequently correlating the widths with projections of PCR3BP energy surfaces onto the osculating eccentricity e versus semi-major axis a plane. The directly computed PCR3BP-based stable resonance zone widths are compared with semi-analytical predictions [1,17,18]. Moreover, the orbits of current xGEO spacecraft like TESS, IBEX, and Spektr-R, obtained via their two-line element (TLE) sets, are projected onto the (a, e) plane to ascertain their positioning within stable or unstable resonance regions. The perigee mappings derived from higher-fidelity ephemeris propagations of TESS, IBEX, and Spektr-R are superimposed onto the Poincaré map and (a, e) plane, further validating the PCR3BP stable resonance widths and chaotic resonance zones.

This paper is organized into nine sections. Section I introduces the problem's motivation and reviews relevant prior research. Section II provides a concise overview of the CR3BP. Section III outlines key aspects of Poincaré maps, focusing on stable and unstable periodic orbits and on defining stable resonance widths and (larger) chaotic resonance regions. Section IV examines MMRs in xGEO, highlighting both stable and unstable periodic orbits. Section V describes the methodology for computing unstable resonant orbits and their stable and unstable manifolds. Section VI summarizes findings from a semi-analytical approach to MMR widths. Section VII discusses the methodology to determine resonance widths and chaotic zones, maps them onto the (a, e) plane, and compares them with semi-analytical widths and TLEs of TESS, IBEX, and Spektr-R. Section VIII analyzes the high-fidelity trajectories of TESS, IBEX, and Spektr-R using Jet Propulsion Laboratory (JPL) Horizons ephemeris data and a Cowell four-body propagation, mapping them onto (a, e) and (ϖ, a) planes. Finally, Sec. IX provides a summary of the paper's main results.

II. Planar Circular Restricted Three-Body Problem

The PCR3BP is the simplest model for motion in cislunar space whose dynamics capture the main qualitative features of the true motion. It describes the motion of a massless spacecraft relative to two primary bodies (e.g., Earth and Moon), viewed in a rotating reference frame centered at the center of mass (barycenter) of the two primaries. The PCR3BP assumes that both primaries move in circular orbits with constant angular velocity about their barycenter and that the spacecraft motion is coplanar with their orbits.

For the equations of motion of the PCR3BP, we choose normalized units such that the distance between the two masses m_1 and m_2 is 1, their combined mass is 1, and their orbital period about the barycenter (the sidereal period T_m) is 2π. The only parameter of the system dynamics is then the mass ratio μ, defined as $m_2/(m_1 + m_2)$. For the Earth–Moon system, we use $\mu = 1.2150584270571545 \times 10^{-2}$. We choose a coordinate frame rotating with the two massive bodies as in Fig. 1 (left), centered at their barycenter with m_1 and m_2 lying on the x axis at $(-\mu, 0)$ and $(1 - \mu, 0)$, respectively. The PCR3BP second-order differential equations of motion for the spacecraft in normalized units are then

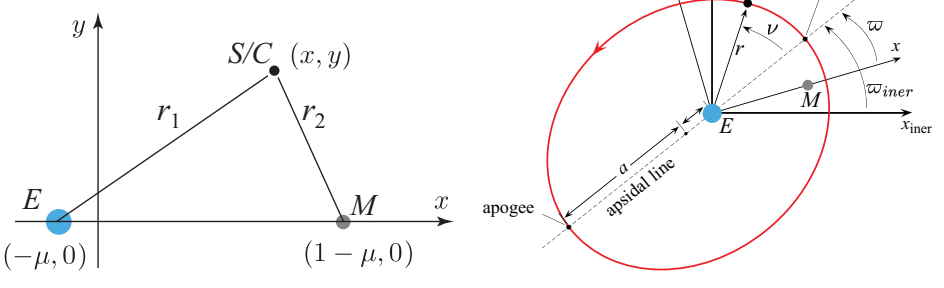

Fig. 1 Left: nondimensional barycentered corotating (x,y) frame. Right: the geocentric osculating orbital elements.

$$\ddot{x} - 2\dot{y} = x - (1-\mu)\frac{x+\mu}{r_1^3} - \mu\frac{x-1+\mu}{r_2^3},$$
$$\ddot{y} + 2\dot{x} = y - (1-\mu)\frac{y}{r_1^3} - \mu\frac{y}{r_2^3} \tag{1}$$

where $r_1 = \sqrt{(x+\mu)^2 + y^2}$ is the distance from the spacecraft to m_1 and $r_2 = \sqrt{(x-1+\mu)^2 + y^2}$ is the distance to m_2. In general, we refer to a point in the four-dimensional, phase-space manifold $\mathcal{M}$ as X. This point can be written in terms of the rotating-frame Cartesian coordinates given previously, $X = (x, y, \dot{x}, \dot{y})$. Alternatively, in the geocentric part of $\mathcal{M}$, one can use instantaneous (i.e., osculating), geocentric orbital elements, for example, $X = (a, e, \ell, \varpi)$, where a is the semi-major axis, e is the eccentricity, ℓ is the mean anomaly, and ϖ is the synodic longitude of perigee with respect to the rotating frame positive x axis, as depicted in Fig. 1 (right). It also illustrates the distinction between synodic longitude of perigee ϖ and inertial longitude of perigee ϖ_{iner}.

The Jacobi constant is proportional to the negative of the Hamiltonian energy of the system and is a constant of motion of the CR3BP equations. In other words, for an initial condition $X \in \mathcal{M}$, this scalar value does not change along the trajectory. The formula we use for the Jacobi constant of the planar problem is[¶]

$$\mathcal{C}(x, y, \dot{x}, \dot{y}) = x^2 + y^2 + 2\left(\frac{1-\mu}{r_1} + \frac{\mu}{r_2}\right) - (\dot{x}^2 + \dot{y}^2) \tag{2}$$

Let $\mathcal{M}_C$ be the energy manifold or energy surface given by setting the Jacobi integral (2) equal to a constant; that is,

$$\mathcal{M}_C = \{X \in \mathcal{M} | \mathcal{C}(X) = C = \text{constant}\} \tag{3}$$

The surface $\mathcal{M}_C$ can be considered as a three-dimensional manifold embedded in the four-dimensional phase space $\mathcal{M}$. Any PCR3BP trajectory starting in $\mathcal{M}_C$ will remain therein for all time, so one can study PCR3BP dynamics restricted to each 3D manifold $\mathcal{M}_C$ separately. For the geocentric portion of $\mathcal{M}_C$ interior to the Moon's orbit, dimensionality can be further reduced by using a two-dimensional Poincaré surface of section, described in Sec. III.

The Tisserand approximation to the Jacobi constant in geocentric orbital-element space in the CR3BP model is

$$C(a, e, i) = \frac{1}{a} + 2\sqrt{a(1-e^2)}\cos i + O(\mu) \tag{4}$$

which dynamically limits the range of motion a nonmaneuvering spacecraft is capable of, depicted using the geocentric, osculating orbital elements: semi-major axis a, eccentricity e, and inclination i. In the PCR3BP, the inclination is set to zero ($i = 0$). The terms of order μ, $O(\mu)$, will be ignored when the Tisserand approximation is used to plot projections of $\mathcal{M}_C$ onto (a, e) space, which appear as curves, referred to as *Tisserand curves*.

III. Poincaré Map and Key Dynamical Features

A. Surface of Section at Perigee

In our study, the Poincaré surface of section is defined at perigee crossings, identified when the geocentric mean anomaly ℓ is zero (equivalently, when true anomaly $\nu = 0$). The section, parameterized by the Jacobi constant C, is

$$\Sigma_C = \{X \in \mathcal{M}_C | \ell = 0\} \tag{5}$$

The Poincaré section so constructed is two dimensional and can be represented by two coordinates that can be interpreted in orbital-element space: the semi-major axis a and the synodic longitude of perigee ϖ, the angle between perigee and the Moon's location in the rotating frame (see Fig. 1). As ϖ is an angular variable, in the region of phase space we study, Σ_C has a cylindrical topology, that is, $(\varpi, a) \in S^1 \times I$, where $I \subset \mathbb{R}$ and S^1 is the circle.

In practice, to detect and stop at crossings of Σ_C during numerical integration, one needs a continuous, *real-valued* function on phase space whose value, when evaluated along the trajectory, crosses zero as the trajectory crosses the section. Both MATLAB® and Julia, among other programming languages, allow user-provided functions to terminate numerical integrations. However, note that the mean anomaly ℓ is not a continuous real-valued function on phase space; it is an angle that repeatedly *jumps* from 2π to 0 along a trajectory. Thus, a different function must be used. Instead, we will consider a continuous, real-valued function of ℓ that vanishes at $\ell = 0$, as described in Appendix A.1.

B. Poincaré Map on Poincaré Section

Poincaré maps simplify the study of the PCR3BP by transforming a four-dimensional phase space into a more manageable two-dimensional analysis, elucidating periodic, quasi-periodic, and chaotic behaviors, and revealing the intricate manifold structures that govern the system's dynamics. The section Σ_C represents a two-dimensional surface transverse to the flow inside the energy manifold $\mathcal{M}_C$ (cf. Fig. 2). Let $x_0 \in \mathcal{M}_C$ denote an initial state, not necessarily in Σ_C. The Poincaré map $P(x_0) = s$ corresponds to the first crossing of Σ_C by the trajectory originating at x_0 in a particular direction. The unit vector $\hat{\Sigma}$ gives the sense in which trajectories are crossing Σ_C. In general, we will consider Poincaré mappings of Σ_C to itself:

$$P: \Sigma_C \to \Sigma_C, \quad s \mapsto P(s) \tag{6}$$

We establish important terminology in the following.

Definition 1: The orbit of a point $s \in \Sigma_C$ under P is the set of all the past and future iterates of the point s under the map P; that is, the infinite sequence of points, $\{\ldots, P^{-1}(s), s, P^1(s), P^2(s), \ldots\}$, also denoted as $\mathcal{O}(s)$. See Figs. 2 and 3 (left) for examples of points and their iterates under the map P. Note that the orbit of s is the same as the orbit of $P^k(s)$ for all $k \in \mathbb{Z}$, and all represent the same continuous *trajectory* within the energy manifold $\mathcal{M}_C$.

Some orbits of P contain only a finite number of distinct points. These correspond to periodic orbits of P, in the sense that the sequence repeats after a minimum integer $n \geq 1$ number of iterates.

Definition 2: A periodic orbit of P is a finite sequence of points $\mathcal{O}(p_n) = \{p_1, \ldots, p_n\}$ such that $p_k = P(p_{k-1})$ for $2 \leq k \leq n$ and $p_1 = P(p_n)$. The period-n points $\mathcal{O}(p_n)$ represent a continuous periodic PCR3BP trajectory, a closed loop, within the energy manifold $\mathcal{M}_C$.

This is a generalization of fixed points, as the state returns to the initial point $p_1 \in \Sigma$ after n iterates of the Poincaré map; that is, $p_1 = P^n(p_1)$, where P^n denotes n compositions of P, $P \circ P \circ \cdots \circ P \circ P$ (n times). For a periodic orbit, we note that each of the points $p_1, \ldots, p_n$ is a fixed point (a period-1 point) under n iterates of the

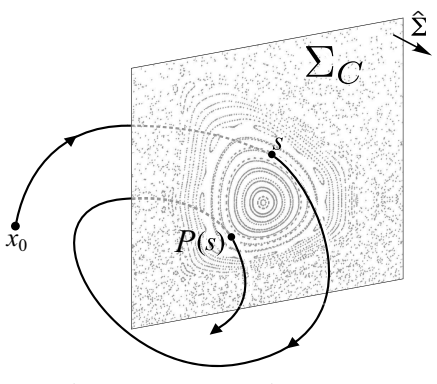

Fig. 2 Poincaré map P on a Poincaré section Σ_C in the CR3BP.

[¶]We note that this definition differs from some authors (e.g., those of Refs. [9,12,19–23]), who add a constant value $\mu(1-\mu)$ so that the Jacobi constant of the L_4 and L_5 points is precisely 3. We adopt the convention most popular in current use among the cislunar astrodynamics community.

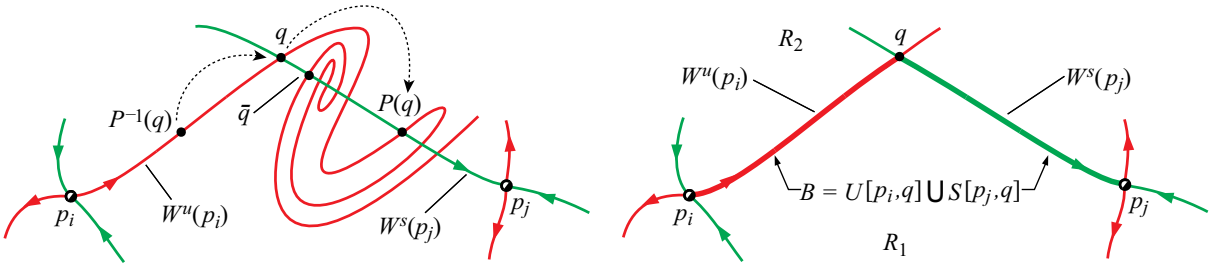

Fig. 3 Left: PIP q and secondary intersection point ($\bar{q}$, not a PIP). Right: BIP q defining a local boundary B separating regions R_1 and R_2.

map, that is, $p_k = \bar{P}(p_k)$, where $\bar{P} = P^n$, and thus we may occasionally refer to each one individually as a fixed point.

If a periodic orbit $\mathcal{O}(p_n)$ is of saddle type, each of the points $p_1, \ldots, p_n \in \mathcal{O}(p_n)$ will have attached stable ($W^s(p_i)$) and unstable ($W^u(p_i)$) invariant manifolds, for $i = 1, \ldots, n$, consisting of orbits of P which tend asymptotically toward $\mathcal{O}(p_n)$ forward or backward in time, respectively. It is known that for two-dimensional (2D) Poincaré maps of two-degrees-of-freedom Hamiltonian systems [24,25] some periodic orbits $\mathcal{O}(p_n)$ are related to a general idea of *resonance*, even beyond just the application to orbital dynamics. If $\mathcal{O}(p_n)$ is of center-type stability, this is a stable resonant orbit. If $\mathcal{O}(p_n)$ is of saddle-type stability, this is an unstable resonant orbit. It should be noted that all members $p_1, \ldots, p_n$ of a periodic orbit have the same stability type.

Let us focus for now on an unstable resonant orbit. There is a systematic way to obtain a *resonance zone* (or, as mentioned earlier, the chaotic resonance zone corresponding to the resonance) via the stable and unstable manifolds of $\mathcal{O}(p_n)$. We first must define a certain type of intersection between the stable and unstable manifolds of $\mathcal{O}(p_n)$. As the stable and unstable manifolds $W^s(p_i)$ and $W^u(p_j)$ are one-dimensional curves within the two-dimensional Poincaré section Σ_C, they will generally intersect transversally in points.** An intersection point of the stable and unstable manifolds of the saddle-type periodic orbit $\mathcal{O}(p_n) = \{p_1, \ldots, p_n\}$ is termed a primary intersection point (PIP), denoted by q in Fig. 3 (left), if it meets the following criteria.

Definition 3: Suppose $q \in W^u(p_i) \bigcap W^s(p_j)$, where p_i, $p_j \in \mathcal{O}(p_n)$, and let $U[p_i, q]$ denote the segment of $W^u(p_i)$ with endpoints p_i and q and $S[p_j, q]$ denote the segment of $W^s(p_j)$ with endpoints p_j and q. Then, q is called a PIP if $U[p_i, q]$ intersects $S[p_j, q]$ only at the point q (and p_i if $i = j$).

Because PIPs are intersections of stable and unstable invariant manifolds, it follows from their definition that all past and future iterates of a PIP are themselves PIPs. The following lemma is proved by Wiggins [16].

Lemma 1: Suppose $q \in W^u(p_i) \bigcap W^s(p_j)$ is a PIP; then, $P^k(q)$ is a PIP for all $k \in \mathbb{Z}$.

We use PIPs to define *boundaries*, sometimes called separatrices, and subsequently resonance regions. Any PIP can be used to denote a local boundary. All intersections between stable and unstable invariant manifolds of the same periodic orbit mark homoclinic points as they enable homoclinic transfers. For example, q and $\bar{q}$ are a homoclinic points for periodic orbit $\mathcal{O}(p_n)$ in Fig. 3.

Definition 4: Suppose $W^u(p_i)$ and $W^s(p_j)$ intersect in the PIP q. Define $B \equiv U[p_i, q] \bigcup S[p_j, q]$ as a boundary between two sides, region R_1 and region R_2. The PIP is then called a boundary intersection point (BIP).

By convention, for a BIP, we pick the PIP with the shortest arc length of the manifolds, measured from the fixed points to the intersection; that is, the shortest arc length for $U[p_i, q] \bigcup S[p_j, q]$. The BIP and the boundary B it defines allows for the local division of the Poincaré section Σ_C into distinct regions R_1 and R_2, as illustrated in Fig. 3 (right).

**A degenerate case occurs when $W^s(p_i) = W^u(p_j)$, that is, a one-dimensional intersection (an unbroken separatrix), but this case is not considered.

As there are always two branches each for a stable and unstable manifold, we can identify both a *top* and *bottom* boundary. We denote the two branches of the unstable manifold of a period-n point p_i by $W^u_+(p_i)$ and $W^u_-(p_i)$, and similarly for p_j. Referring to Fig. 4, we suppose that $W^u_+(p_i)$ intersects $W^s_+(p_j)$ and $W^s_-(p_i)$ intersects $W^u_-(p_j)$. Choosing BIPs $q^+ \in W^u_+(p_i) \bigcap W^s_+(p_j)$ and $q^- \in W^s_-(p_i) \bigcap W^u_-(p_j)$, we can identify boundaries B^+ and B^- that define a closed region R_1, which we refer to as a *resonance region*.

Within our cylindrical Poincaré section Σ_C, we can have multiple resonance regions. Figure 5 shows an example calculation [22] of two neighboring resonance regions corresponding to neighboring resonant orbits along with their stable (green) and unstable (red) manifolds. *Identify* indicates that the synodic longitude of perigee is an angle that maps back to itself. BIPs are identified (solid black dots), and the *width* of a (chaotic) resonance region containing unstable resonant orbit $\mathcal{O}(p_n)$ is marked as the distance between the BIPs of $\mathcal{O}(p_n)$ having maximum and minimum semi-major axes (the dashed lines in Fig. 5).

Resonance regions represent the dynamical *sphere of influence* of a particular resonance. In the PCR3BP, they contain within them the

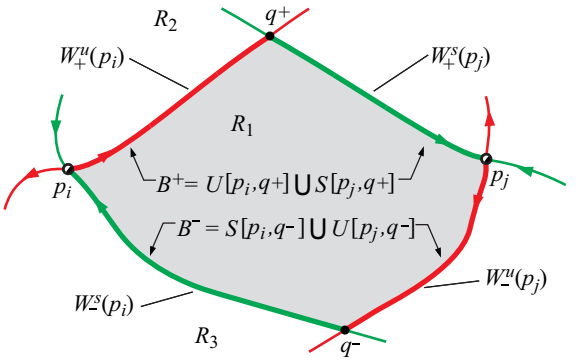

Fig. 4 Construction of a top and bottom boundary to a resonance region R_1.

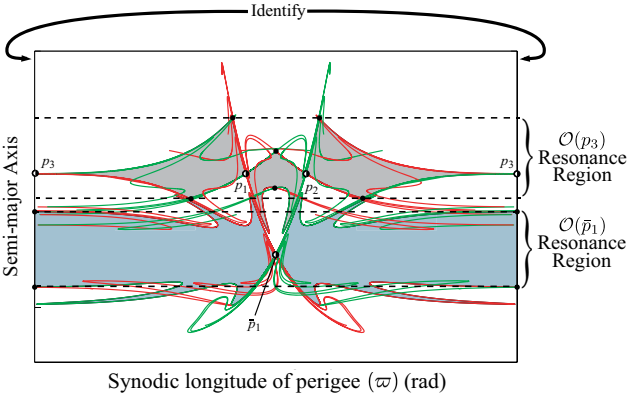

Fig. 5 Resonance regions for a period-3 $\mathcal{O}(p_3) = \{p_1, p_2, p_3\}$ and a neighboring period-1 orbit $\mathcal{O}(\bar{p}_1) = \{\bar{p}_1\}$.

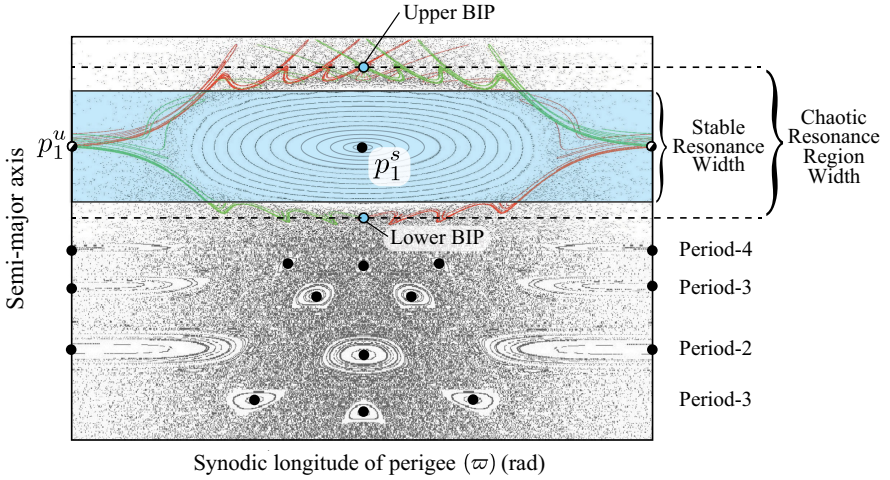

Fig. 6 Stable resonance widths and larger circumscribing chaotic resonance region widths.

corresponding stable resonant periodic orbit and the surrounding stable quasi-periodic orbits, the librational resonant tori. Outside of the largest (outermost) librational torus, there is a *stochastic* or chaotic layer. The stable resonance width is given by the outermost closed curve of the stable resonance island, while the larger chaotic resonant region width is given by the semi-major axis width between the upper and lower BIP. This is illustrated in Fig. 6 which shows an example calculation on a Poincaré section at perigee Σ_C, showing background points: initial conditions followed over several iterates of the map P. The shaded region denotes the stable resonance width (corresponding to stable period-1 resonant orbit p_1^s), and the dashed lines denote the chaotic resonance region (corresponding to its unstable counterpart p_1^u). Other stable period-n points are also shown. The dynamics of motion into and out of the resonance region are determined by lobe dynamics not addressed here [22] but documented elsewhere [11,21,26–28].

Intersections between stable and unstable invariant manifolds of different periodic orbits can occur. For example, suppose $\mathcal{O}(p_n)$ and $\mathcal{O}(\bar{p}_{\bar{n}})$ correspond to two different continuous unstable periodic trajectories in the PCR3BP, as in Fig. 5. Unless constrained by barriers within Σ_C such as rotational invariant curves (RICs) [8,10,29] (quasiperiodic KAM tori that block transport along semi-major axis in the cylindrical phase space of Σ_C), it is possible for there to be intersections between stable and unstable manifolds of $\mathcal{O}(p_n)$ and $\mathcal{O}(\bar{p}_{\bar{n}})$. Such intersections are denoted as *heteroclinic* points and enable heteroclinic transfers. Although not explicitly labeled, one can observe several heteroclinic points in Fig. 5 between the displayed unstable resonant orbits $\mathcal{O}(p_3)$ and $\mathcal{O}(\bar{p}_1)$, that enable heteroclinic transfers.

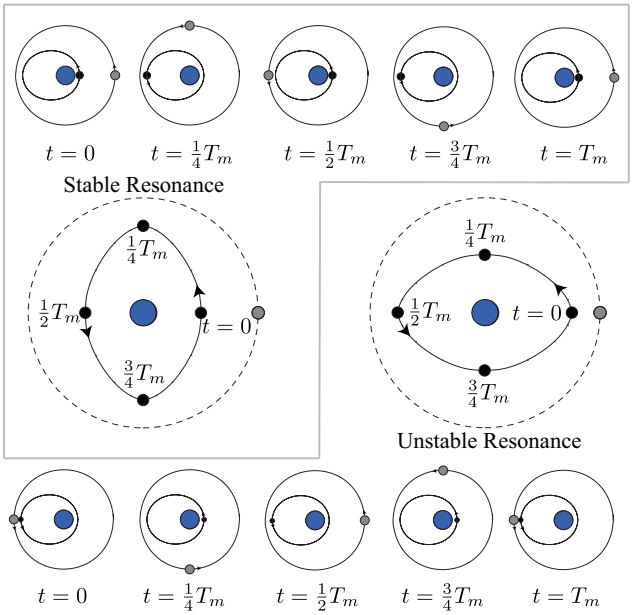

Fig. 7 Top left: configurations of 2:1 stable MMR orbit at fractions of T_m. Bottom right: configurations of 2:1 unstable MMR orbit at fractions of T_m.

IV. Resonances in xGEO

Mean-motion resonances in celestial mechanics result from gravitational interactions among celestial bodies, where their orbital periods create specific integer ratios. For instance, a 2:1 resonance signifies that one body completes two orbits for every single orbit completed by another, thereby influencing the stability and evolutionary trajectories of orbits over extended duration; see Fig. 7. Of particular interest for space domain awareness within cislunar xGEO space are recurrent pathways between Earth and the Moon's orbit. Resonant orbits, being periodic or quasi-periodic by nature, have a rich history in mission design applications, particularly within the Earth–Moon system.

A mean-motion resonance, denoted as $k{:}k_m$, is defined by the ratio of orbital periods, where k and k_m are coprime positive integers, respectively, representing the number of spacecraft and Moon orbits completed around the Earth in equal time in an Earth-centered inertial frame. In this paper, we study interior resonances, where $k > k_m$. Expressed in terms of the inertial-frame period of the spacecraft T and the sidereal period of the Moon, we have an approximate relationship, $T/T_m \approx k_m/k$. When observed within the context of the CR3BP, resonant orbits do not adhere strictly to the integer ratio k_m/k; thus, $T/T_m \approx k_m/k$ is approximate. Instead, a spacecraft completes approximately k revolutions around the Earth in the time it takes the Moon to complete k_m revolutions. In terms of the Poincaré map and section described previously, (P, Σ_C), a resonant orbit is a period-k orbit of P that takes approximately k_m sidereal lunar periods of physical time. These orbits can be found via differential-correction procedures that are well known in the literature [22].

Resonant orbits can be categorized as either stable (for interior resonances, characterized by a perigee oriented toward the Moon in the rotating frame) [30] or unstable (with an apogee oriented toward the Moon), as shown in Fig. 7. A stable resonant orbit when linearized about its corresponding fixed points on the map, $\mathcal{O}(p_n)$, will have center-type stability. An unstable resonant orbit when linearized about its corresponding fixed points on the map, $\mathcal{O}(p_n)$, will have saddle-type stability. Unstable resonant orbits can be exploited in mission design for transfer scenarios, while stable resonant orbits, as demonstrated by missions such as IBEX and TESS, ensure sustained operational stability. For example, IBEX

eventually transitioned into a stable 3:1 resonant orbit, allowing for its prolonged mission duration [30]. Similarly, TESS has maintained a stable 2:1 resonant orbit since its inception via a lunar flyby [31].

V. Unstable Periodic Orbits and Manifolds

In the PCR3BP, to understand the structure of unstable resonant orbit families and the heteroclinic dynamics induced by them, one needs to compute the corresponding periodic orbits as well as their stable/unstable manifolds. To compute a family of $k{:}k_m$ unstable periodic orbits in the Earth–Moon PCR3BP, we start with an orbit state from the Earth Kepler problem having semi-major axis a such that $(a/a_m)^{3/2} = (k_m/k)$, where $a_m = 1$ in nondimensional units, and initial longitude of periapsis and true anomaly both π (for the interior MMRs considered in this study). This orbit will be symmetric about the x axis and will also be periodic in the rotating Kepler problem (i.e., PCR3BP with $\mu = 0$). Thus, the method of perpendicular x-axis crossings can be used to numerically continue this Keplerian orbit to the true value of $\mu = 1.2150584270571545 \times 10^{-2}$ for the Earth–Moon system; see, for example, Sec. 2.6.6.2 of Parker and Anderson [32] for details of this method. The same method is then used to continue the resulting PCR3BP orbit through the rest of its orbit family, using the perpendicular orbit x-intercept as the continuation parameter.

Once the periodic orbits in a family $k{:}k_m$ have been computed, the computation of their stable/unstable manifolds is carried out. In particular, we compute the intersection of these manifolds with the previously mentioned perigee Poincaré surface of section Σ_C. Such sections have been used by, for example, Ross and Scheeres [10] and Howell et al. [33] as well; they have better transversality to the PCR3BP flow as compared to other commonly used sections such as $y = 0$. When using such a section, however, the periodic orbit intersection points with the section are not fixed points of the Poincaré map P but become period-k orbits under the map, as discussed in Sec. III. This is because such a $k{:}k_m$ orbit passes through perigee k times during one period, which takes approximately k_m lunar sidereal periods.

The portions of the periodic orbit stable/unstable manifolds lying in the chosen Poincaré section correspond to one-dimensional (1D) curves, one curve for each of the period-k points within the section. To compute these manifolds accurately, we used a parameterization method [34] developed by the second author [35] for computing Taylor-series approximations of periodic orbit stable/unstable manifolds, which was extended from algorithms [36] developed for manifolds of Poincaré map (period-1) fixed points. Although a full description is beyond the scope of this paper, in brief, given an unstable resonant periodic orbit at Jacobi constant C, we solve for a function $W : \{0, \ldots, k-1\} \times \mathbb{R} \to \mathcal{M}_C \subset \mathbb{R}^4$ such that

$$\phi_{\tau(i)}(W(i,s)) = W(i+1 \bmod k, \lambda s) \quad i \in \{0, \ldots, k-1\} \tag{7}$$

where $\phi_t(X)$ is the PCR3BP flow map of a point $X \in \mathcal{M}$ by time t, $\tau(i)$ is the time elapsed between the ith and $(i+1)$th periapsis passes of the periodic orbit being considered, and λ is the kth root of the monodromy matrix eigenvalue corresponding to the stable/unstable manifold. Note that the $\phi_{\tau(i)}$ are *not* Poincaré maps, but fixed-time maps. Equation (7) can be solved recursively by expressing W as a set of Taylor series depending on the integer i,

$$W(i,s) = \sum_{\bar{m}=0}^{\infty} W_{\bar{m}}(i) s^{\bar{m}} \quad i \in \{0, \ldots, k-1\} \tag{8}$$

where $W_0(i) = p_{i+1}$ are the periapsis period-k points of the periodic orbit and $W_1(i)$ are scaled eigenvectors of the periodic orbit monodromy matrix at each of its periapsis passages, with $W_{\bar{m}}(i)s^{\bar{m}}$ for $\bar{m} \geq 2$ corresponding to higher-order terms in the stable/unstable manifold approximation.

The k curves parameterized by W lie near but not on Σ_C, the periapsis section of interest. Thus, to finally compute the manifolds on the section, one simply numerically integrates dense grids of points from those curves either backward or forward to the section. Then, further applications of the Poincaré map P either forward or backward in time are used to respectively globalize the full unstable and stable manifolds. As usual, for each fixed Jacobi constant value C, one can plot these Poincaré map manifolds of various orbits at that C value using just 2D coordinates on Σ_C. Intersections of the 1D manifold curves $\{W_{\pm}^{u,s}(p_i)\}$ will provide the geometry (e.g., PIPs, BIPs, homoclinic points, heteroclinic points) as discussed in Sec. III.

VI. Semi-Analytical Approach to Identify Resonance Widths

Standard tools have been developed in celestial mechanics to calculate the width (strength) and location of MMRs, under the perturbed-Hamiltonian formulation [1,37,38]. They all invariably employ an expansion of the Hamiltonian around each resonant location and a *canonical transformation* to reduce the Hamiltonian to a system with only one single harmonic (i.e., normal-form reduction). Although the mathematical developments here are straightforward, they can be algebraically quite complicated, especially for distant xGEO orbits of high eccentricity and inclination.

The semi-secular Hamiltonian describing the resonant dynamics near the $k{:}k_m$ MMR is [18]

$$\begin{aligned} \mathcal{K}(a,\sigma) &= -\frac{\mu_e}{2a} - n_m \frac{k}{k_m}\sqrt{\mu_e a} - \mathcal{R}(a,\sigma), \\ \mathcal{R}(a,\sigma) &= \frac{1}{2\pi k_m}\int_0^{2\pi k_m} R(\lambda_m, \lambda(\lambda_m,\sigma))\,\mathrm{d}\lambda_m \end{aligned} \tag{9}$$

where $\mu_e = Gm_e$ is the Earth's gravitational parameter; $n_m = \sqrt{\mu_e/a_m^3}$ is the Moon's mean motion, λ_m and λ are the Moon and satellite mean longitudes, respectively; and R is the Moon's disturbing function

$$R = \mu_m\left(\frac{1}{|\boldsymbol{r}_m - \boldsymbol{r}|} - \frac{\boldsymbol{r}\cdot\boldsymbol{r}_m}{r_m^3}\right) \tag{10}$$

The resonant disturbing function $\mathcal{R}(a,\sigma)$ can be written as a series expansion of cosines whose critical arguments are of the type

$$\sigma = k_m\lambda - k\lambda_m + \gamma \tag{11}$$

where γ is a slowly evolving angle defined by a linear combination of the longitudes of the ascending nodes Ω_{iner} and longitudes of perigee $\varpi_{\text{iner}} = \Omega_{\text{iner}} + \omega_{\text{iner}}$ of the satellite and Moon.

Gallardo [17,18] uses a numerical computation for the averaging in Eq. (9), assuming that the Moon's orbit is Keplerian and lies in the ecliptic plane and taking for the spacecraft the semi-major axis corresponding to the nominal position of the resonance and assuming the satellite's eccentricity, inclination, periapsis, and node are fixed during the period of time in which the integral is calculated. This is justified in the asteroid case by the otherwise slow evolution time scale of (e, i, ω, Ω), as compared to the oscillations of a and σ.

For the Earth–Moon system, the resonance widths calculated using Gallardo's algorithm are shown in osculating semi-major axis-eccentricity (a, e) space in Fig. 8, using the mean orbit of the Moon (i.e., $a_m = 383397.7725$ km, $e_m = 0.055545526$) as input parameters for the perturber [39]. The satellite's inclination was set to zero, and the tolerance criterion was set to 2.0 R_H (twice the Moon's Hill radius, R_H), to avoid erroneous results that occur near close encounters (see Ref. [18] for a more detailed discussion). The phase-space structure of the widths of 3:1 and 2:1 resonances generally resemble those in the small-body context (e.g., hourglass shapes) [40], but the 1:1 (coorbital resonance) is dramatically over predicted with its width encompassing the entire lunar Hill sphere [$R_H = 0.1587$ dimensional units (DU), in semi-major axis ranging from 0.83 to 1.15 DU].

The other resonances appearing in Gallardo's *atlas*, limited herein to order 5, will not be discussed further. The time histories of

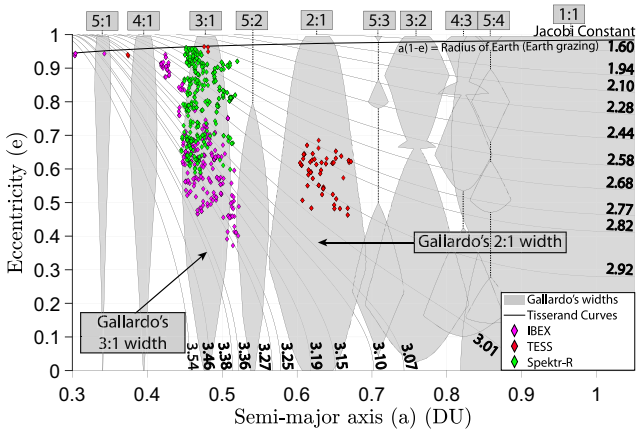

Fig. 8 TLEs of TESS, IBEX, and Spektr-R, superimposed on Gallardo's widths in the (a,e) plane.

notable xGEO resonant satellites (IBEX, Spektr-R, and TESS), obtained from TLE data,[††] are overlaid; it can be observed that TESS lies within the predicted libration zone of the 2:1, but the predicted 3:1 width does not fully encompass the other spacecraft.

VII. Direct Identification of Resonance Widths and Chaotic Zones

We calculate and plot intersections of numerous PCR3BP orbits with the Poincaré section Σ_C for a range of Jacobi constants, revealing various resonances; see the (ϖ, a) plane in Fig. 9, in which ϖ is the longitude of perigee in the rotating frame. The most prominent resonances are the 2:1, 3:1, and 4:1 MMRs (4:1 MMR is identified but will not be discussed further). The stable resonance zones are particularly apparent as *islands* of concentric closed curves surrounding center points that are stable period-2, period-3, and period-4 orbits, respectively. The closed curves surrounding the stable fixed points are stable quasi-periodic librational tori (recall Sec. IV). Surrounding these resonance islands are regions of chaos. These regions are not featureless. Instead, the template of the motion is given by the corresponding unstable MMR periodic orbits, which appear as saddle-type period-k points on the Poincaré section Σ_C. Using the method of Sec. V, these periodic orbits and their manifolds are computed. The stable and unstable manifolds intersect to form homoclinic and heteroclinic tangles, which provide the paradigm for understanding chaos in the CR3BP [9,41].

The existence of a particular mean-motion resonance can be identified by examining the Poincaré section, which also reveals its strength (width). Resonance widths as defined in Sec. III (Fig. 6), are shown for the 3:1 (shaded yellow) and 2:1 (shaded cyan) MMRs on Poincaré maps computed for $C = 3.00, 3.05, 3.10, 3.15$ in Fig. 9. The extent of the outermost invariant circle of the stable island in semi-major axis is identified visually to compute the resonance widths.

The influence of each resonance region extends beyond the outermost stable resonant librational torus regions to the *separatrix*, the boundary formed by the intersection of stable and unstable manifolds described in Sec. III (see Fig. 5). Focusing on the MMR bands, we use the methods of Sec. III to identify BIPs and designate the boundary of each (chaotic) resonance region. BIPs defining the chaotic zones are depicted on the same Poincaré maps in Fig. 9. For $C \geq 3.10$ the upper 2:1 BIP disappears. In fact, we see a *swirling* of manifolds that is a consequence of interaction with the L1 Lyapunov stable manifold cut resulting in trajectories *exiting* the Poincaré section in the Earth realm, entering the Moon realm, and then reemerging in the Earth realm.

While the resonances are identified and visualized in the (ϖ, a) space, we also aim to represent them in the (a, e) plane for direct comparison with space-object distributions and the semi-analytical resonance widths shown in Fig. 8. The points from the Poincaré section, which exist in the three-dimensional (a, e, g) space for each C, can be projected onto the (a, e) plane, as illustrated in Fig. 10. In this figure, the stable resonance widths (shaded yellow and cyan) and the BIPs that bound the resonance zones are delineated. As discussed in Sec. II, Tisserand curves provide an approximation of the projection of the energy surface $\mathcal{M}_C$ onto the (a, e) plane. For each Jacobi constant C in Fig. 10, we include the corresponding Tisserand curve to highlight the agreement, particularly for smaller semi-major axes.

The results in Fig. 10 illustrate our method, but the number of Jacobi constants is sparse. To get a fuller picture of the (stable) resonance widths and the (chaotic) resonance regions, Poincaré sections were computed for Jacobi constant values C ranging from 1.60 to 3.54 in increments of $\Delta C = 0.02$. As shown in Fig. 11 (top), the Poincaré section points were projected onto the (a, e) plane, marking resonance widths and chaotic resonance zones (via BIPs) for the 2:1 and 3:1 resonances. The stable-band boundaries appear jagged due to discretization effects. Widths are assembled from resonance islands computed at discrete Jacobi constants with additional small irregularities from manual delineation and finite grid resolution. The family of prograde stable 3:1 resonant periodic orbits exists for $C = 2.10$ to 3.47, with trajectories resulting in Earth collisions for $C \leq 2.44$. Similarly, the prograde stable 2:1 resonant periodic orbit family begins at $C = 1.6$, with Earth-impacting orbits occurring for $C \leq 1.94$. As our current manifold computation methods do not incorporate Levi-Civita regularization, accurate manifold computations for unstable resonant orbits approaching or colliding with Earth were not possible. Consequently, manifolds are plotted starting only from $C = 2.44$.

The stable widths obtained by using the full PCR3BP model are comparable to those computed using Gallardo's algorithm, as seen in Fig. 11 (bottom). However, Gallardo's widths are computed from the resonance center (stable equilibrium) to the maximum libration, capturing only the stable libration zones. This method neglects the deformation of resonance separatrices due to interactions with neighboring resonant harmonics, a significant effect at higher mass ratios. Consequently, when compared to the chaotic resonance zones indicated by the BIPs, Gallardo's algorithm substantially underestimates the true region of influence of the 2:1 and 3:1 unstable resonances.

Specifically, the PCR3BP stable width for the 2:1 resonance appears larger than Gallardo's approximation for near-zero and near-unity eccentricities but are slightly smaller for eccentricities in between. For eccentricities approaching unity, higher-order resonances (also known as *sticky islands*) form around the primary resonance island. The invariant curves start surrounding these sticky islands and contribute to the increased widths at high eccentricities, a phenomenon Gallardo's algorithm does not capture. Moreover, the shape of the 2:1 resonance does not show the characteristic shape seen in other CR3BP-based resonance-width computations [2,37]: a largest width near some eccentricity $0.3 \leq e \leq 0.7$ tapering to significantly smaller widths as e approaches 0 and 1. We note that earlier work tended to assume that resonance widths should be along lines of constant semi-major axis in the (a, e) plane [37], which does not consider the *tilt* of the energy surface (as approximated by Tisserand curves).

The regions of influence of 2:1 and 3:1 unstable resonance regions, as represented by BIPs, nearly touch in the region between them, indicating possible heteroclinic connections which are in fact observed in Fig. 9. A detailed analysis of the corresponding heteroclinic transfer trajectories is provided in our recent related work [42]. The stable resonance zones of 2:1 and 3:1 span approximately 28,328 and 20,281 km in the semi-major axis, respectively, when averaged across all Jacobi constants. The regions of influence of 2:1 and 3:1 unstable resonances respectively span approximately 83,982 and 34,619 km in the semi-major axis, when averaged across all Jacobi constants. These regions encompass numerous higher-order resonances, suggesting the potential for multiple free transfers between different order resonances.

As done previously in Fig. 8, time histories of IBEX, TESS, and Spektr-R are overlaid in Fig. 12. The PCR3BP resonance widths and

[††]Information available online at www.space-track.org [retrieved 10 March 2023].

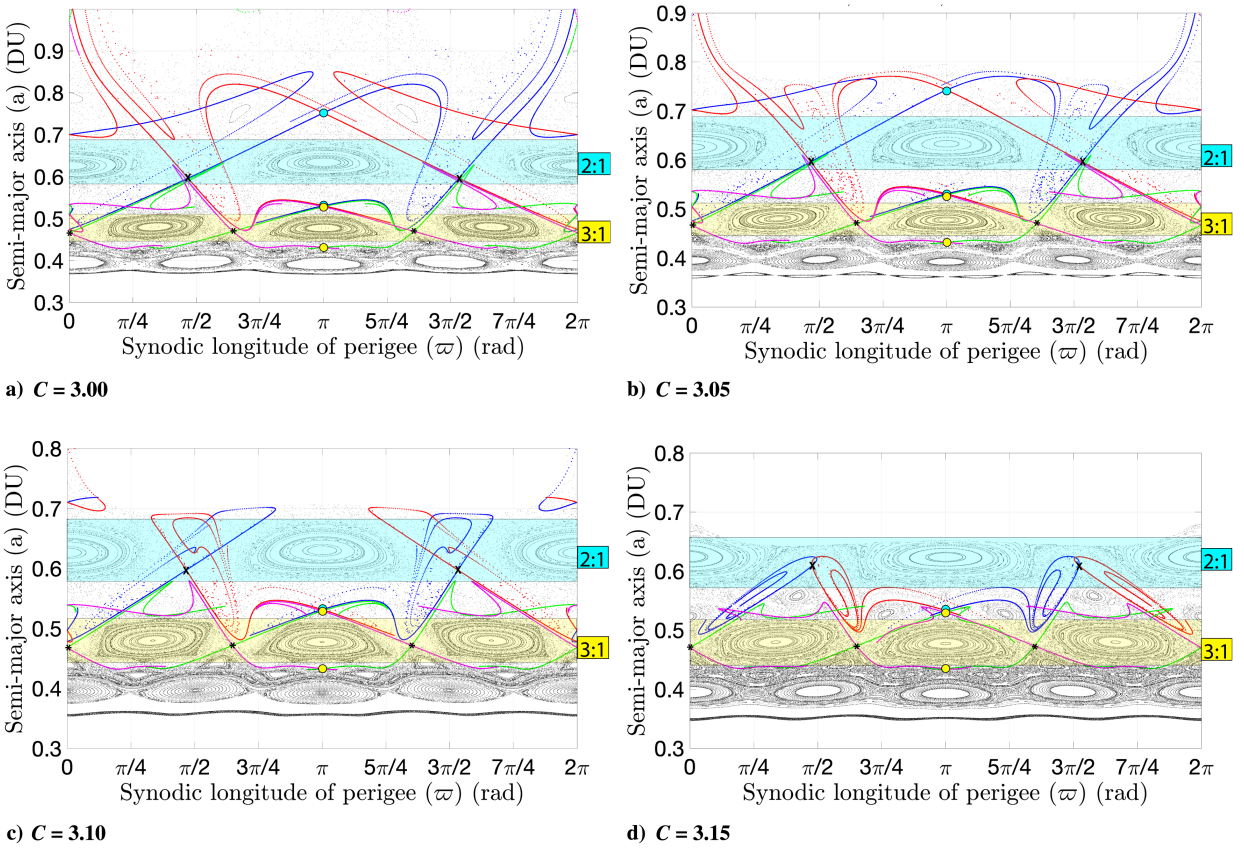

Fig. 9 Poincaré sections depicting resonance widths and chaotic zones of the 2:1 and 3:1 MMRs.

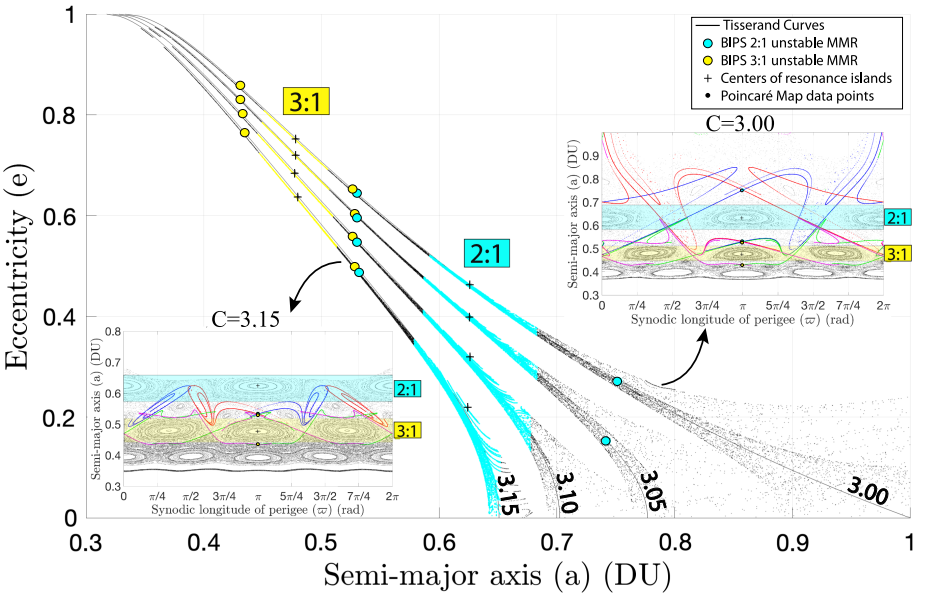

Fig. 10 (a,e) projection of resonance widths and chaotic zones of the 2:1 and 3:1 MMRs.

chaotic zones effectively encompass these xGEO space objects. In contrast, the semi-analytical resonance widths approximation inadequately represents the locations of the spacecraft. Notably, the PCR3BP resonance zones in (a, e) can accurately discern the resonant dynamical character of even noncoplanar spacecraft (discussed in detail in Sec. VIII), underscoring its utility in providing fundamental insights into spacecraft dynamics in cislunar space. Using these resonance widths facilitates the determination of whether a spacecraft is within a stable or chaotic orbital regime, thereby aiding in mission analysis and prediction of its future orbital evolution.

For instance, IBEX's nominal orbit exhibited chaotic behavior due to lunar perturbations, prompting a transfer to a stable 3:1 resonant orbit with the Moon [30]. A comprehensive understanding of chaotic dynamics in such environments would have been valuable during the mission's early design phases. This understanding has partly informed the orbital design of missions like TESS [31]. Although significant challenges remain in comprehending lunar secular and mean-motion resonances, progress in discerning the influence of specific resonances, such as the 2:1 and 3:1 MMRs, through the PCR3BP, contributes to advancing our understanding of these important lunar resonances.

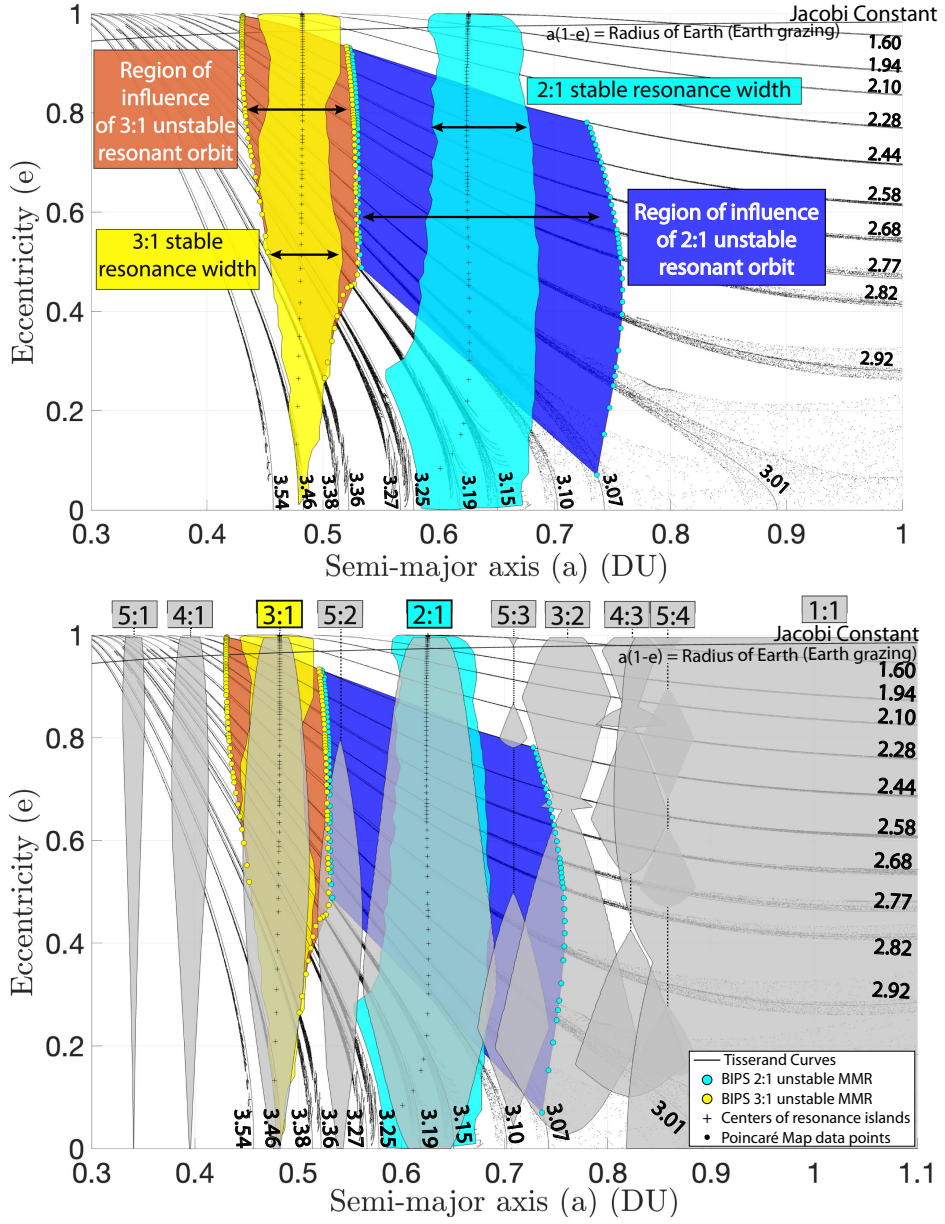

Fig. 11 Top: resonance widths and chaotic resonance zones for $C = 1.6$ to $C = 3.54$ ($\Delta C = 0.02$). Bottom: PCR3BP widths overlapped onto Gallardo's widths.

VIII. Comparison with Ephemeris Model

Figure 13 shows planar projections of ephemeris propagations of resonant spacecraft: TESS is situated in a stable 2:1 MMR, mostly occupying a larger quasi-periodic torus; IBEX is located in a stable 3:1 MMR; and Spektr-R navigates in unstable regimes, thus having a chaotic trajectory. The orbital trajectories of TESS, IBEX, and Spektr-R, as described by their TLEs, predominantly fall within the stable resonance widths of the PCR3BP, as illustrated in Fig. 12. TLEs provide snapshots of a satellite's orbital elements at specific epochs, typically referenced to the ascending node. Thus, their comparison with PCR3BP stable resonance widths can serve as a preliminary validation. However, TLEs are inherently sporadic and do not accurately represent osculating elements at or near the perigee. To address this limitation, the trajectories of TESS, IBEX, and Spektr-R are propagated using high-fidelity Sun–Earth–Moon–satellite ephemeris models (Horizons and Cowell's four-body propagator) enabling the determination of perigee crossings to map onto the PCR3BP widths (a, e) plane and on the Poincaré maps' (ϖ, a) plane. In the spatial CR3BP, the synodic longitude of perigee is defined as the inertial argument of perigee plus the synodic angle between the Earth–Moon line and the ascending-node direction ($\varpi = \Omega + \omega$).

For TESS and Spektr-R, trajectory propagation is conducted using JPL Horizons data for 2-year intervals, from initial epoch 1 November 2020 for TESS and 28 February 2013 for Spektr-R. A data extraction time step of 10 min is selected after confirming negligible variations in near-perigee states with finer data extraction time steps up to 1 min. Data points are extracted with respect to the International Celestial Reference Frame, centered at the Earth and ecliptic reference plane. Near-perigee crossings are identified based on minimum distance and the condition $\boldsymbol{r} \cdot \boldsymbol{v} = 0$. The inertial perigee states are then converted to synodic states using the methodology described in Appendix A.2. The Jacobi constant (for each state), calculated using spatial states, is averaged over all states to account for its variation in the high-fidelity model, after which a two-dimensional plot of Poincaré map orbit points is computed at that same spatial Jacobi constant value. The spacecraft synodic perigee crossings converted into geocentric osculating orbital elements are then mapped onto the Poincaré map plot and PCR3BP widths. Additionally, spatial CR3BP propagation of the initial Horizons/Cowell's perigee state is performed, and subsequent perigee crossings are mapped onto the Poincaré map for comparison. For IBEX, Horizons data are unavailable, necessitating trajectory

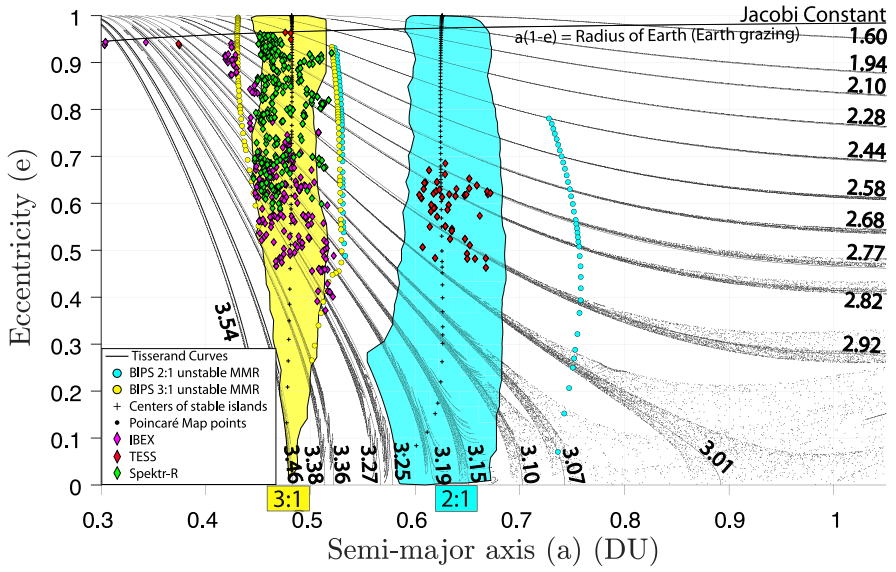

Fig. 12 TLEs of TESS, IBEX, and Spektr-R (from Fig. 8) superimposed on PCR3BP-based widths.

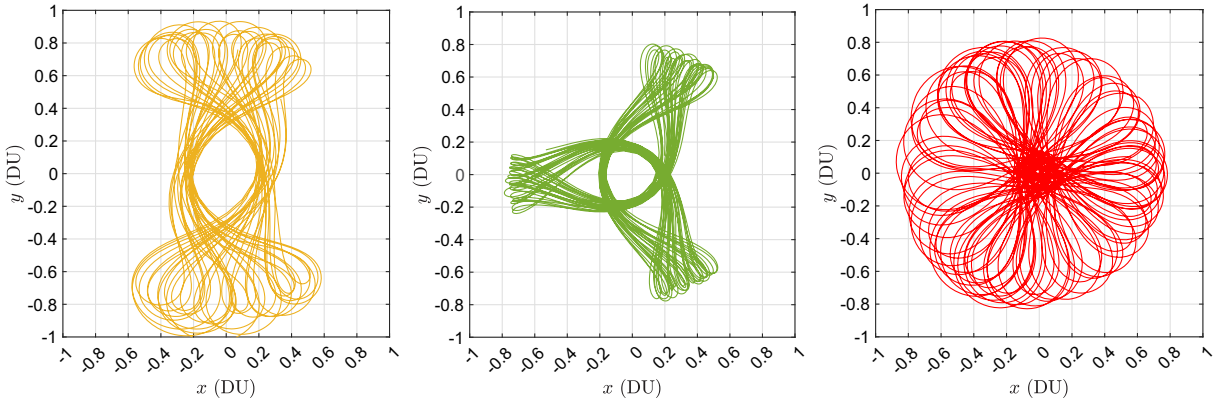

a) TESS: 11.01.2020–11.01.2022 **b) IBEX: 02.28.2013–03.01.2015** **c) Spektr-R: 02.28.2013–02.28.2015**

Fig. 13 Ephemeris trajectories converted into synodic states and projected onto the Earth–Moon *xy* plane.

propagation using Cowell's four-body propagator over 2 years (28 February 2013 to 1 March 2015), with the initial condition for IBEX being that reported by Ref. [30]. Perigee states are identified using MATLAB®'s event functionality, converted to synodic states, and mapped similarly onto the Poincaré map and PCR3BP widths.

Figure 14 compares TLEs and the perigee states derived from high-fidelity propagation of TESS, IBEX, and Spektr-R over 2 years. The results indicate that the perigee states of TESS and IBEX, which are associated with stable 2:1 and 3:1 resonances, respectively, largely align with the stable PCR3BP resonance widths.

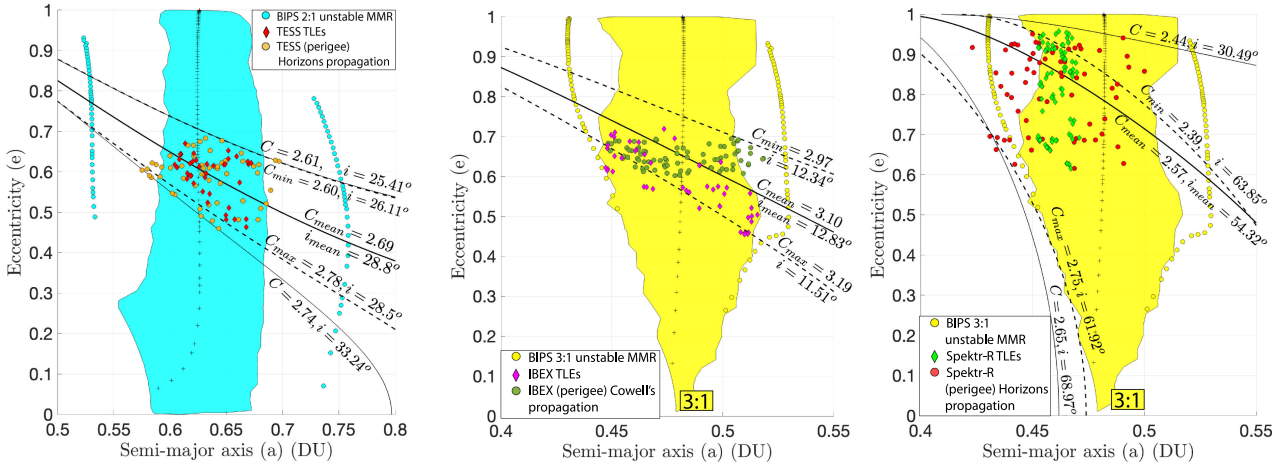

a) TESS: 11.01.2020–11.01.2022 **b) IBEX: 02.28.2013–03.01.2015** **c) Spektr-R: 02.28.2013–02.28.2015**

Fig. 14 TLEs and ephemeris perigee crossings on PCR3BP widths, with inclined Tisserand curves.

However, some data points fall outside the widths attributable to including higher-fidelity effects in the propagation. Despite these deviations, the PCR3BP widths approximate the underlying fundamental dynamical framework. Figure 14c indicates that Spektr-R's perigee states lie predominantly within the chaotic zone of the 3:1 resonance. We distinguish the resonant (fast) dynamics, involving semi-major axis and the resonant angle, from the secular (slow) dynamics governing eccentricity, inclination, longitude of ascending node, and argument of perigee. In the case of Spektr-R, likely both modes exhibit chaotic dynamics; in the resonant dynamics case because of its location within the 3:1 unstable phase space region and in the secular dynamics case on account of von Zeipel–Lidov–Kozai oscillations [43,44] due to its significantly high ecliptic inclination ($i_{\text{mean}} = 54.32$ deg with respect to lunar plane). This dual origin explains the observed scatter of perigee states beyond the stable-band envelopes and remains consistent with Tisserand constraints as described further.

The Tisserand curves, incorporating inclination relative to the Earth–Moon plane, are plotted in Fig. 14 for the maximum and minimum (dashed), mean (bold), and selected intermediate (light) Jacobi constants derived from 2 years of perigee data. A mean Jacobi constant Tisserand curve, combined with the mean inclination with respect to ecliptic plane from 2 years of perigee data, is also included; TESS's is $C_{\text{mean}} = 2.69$, $i_{\text{mean}} = 28.8$ deg, IBEX's is $C_{\text{mean}} = 3.10$, $i_{\text{mean}} = 12.83$ deg, and Spektr-R's is $C_{\text{mean}} = 2.57$, $i_{\text{mean}} = 54.32$ deg. Most data points for TESS and IBEX lie within these established boundaries, with deviations arising from the inherent limits of Tisserand curves in approximating the true energy surface. Notably, cases such as TESS ($C = 2.74$, $i = 33.24$ deg) illustrate how higher-inclination points can fall outside the extreme Jacobi constant boundaries. For IBEX, it is noted that the TLEs during the specified observation period are quite sporadic, contributing to their deviation from the predicted ranges of Tisserand curves. Spektr-R presents a distinctive case characterized with substantial variations in orbital inclinations. Notably, the perigee point corresponding to $i = 30.49$ deg has an $e > 0.9$, whereas data points corresponding to $i = 68.97$ deg have $e < 0.7$. This observed tradeoff between eccentricity and inclination illustrates the effect of secular resonances.

Mapping perigee crossings to the (a, e) plane alone is insufficient to confirm stability of a satellite, as observed in the case of Spektr-R. Instead, the (ϖ, a) plane is also examined to verify alignment of perigee crossings with stable resonant islands on the Poincaré map. Thus, high-fidelity propagated perigee states of these three satellites are mapped onto the respective Poincaré maps computed for averaged Jacobi constants, as shown in Fig. 15 along with the spatial CR3BP propagation of their initial perigee state (marked).

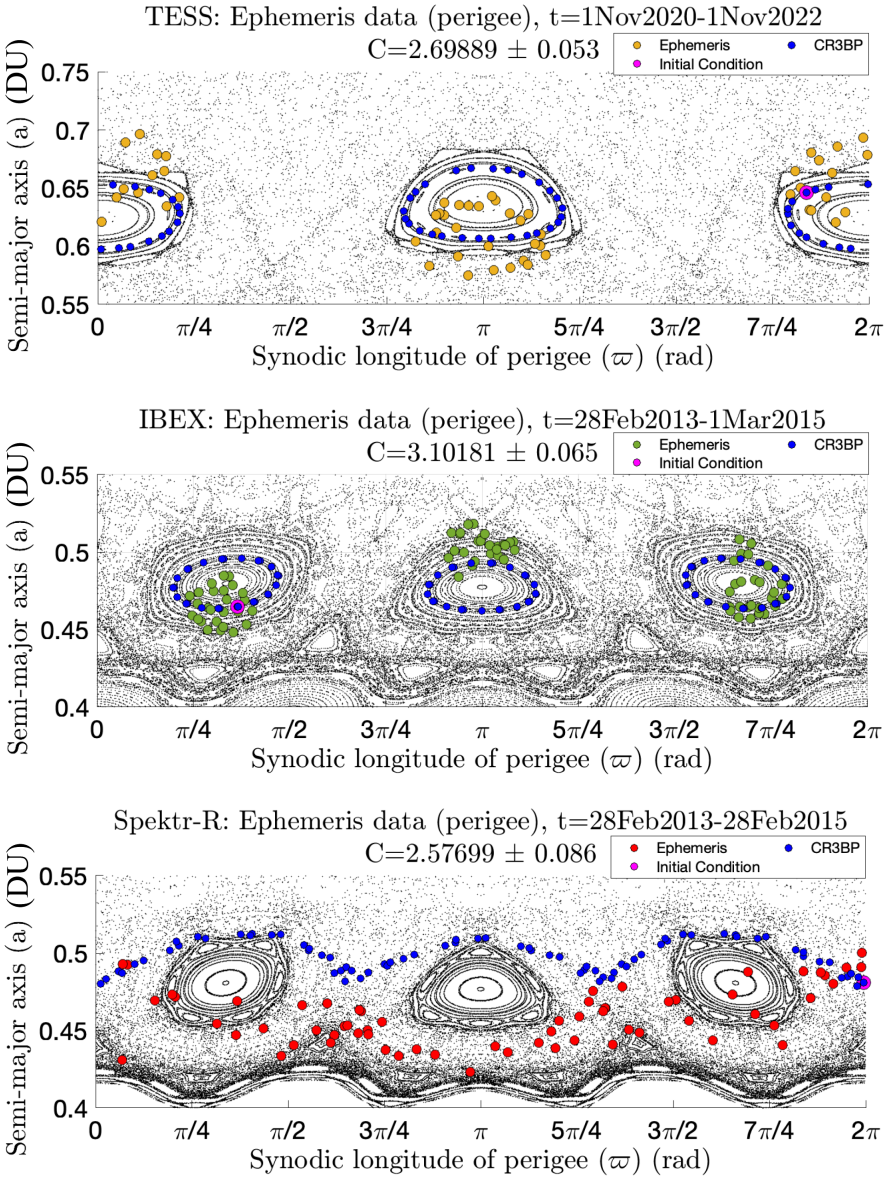

Fig. 15 CR3BP propagation and ephemeris perigee crossings overlaid onto respective Poincaré maps for (top) TESS ($C = 2.69889$), (middle) IBEX ($C = 3.10281$), and (bottom) Spektr-R: ($C = 2.57688$).

The perigee mappings obtained from spatial CR3BP propagations of initial states for TESS and IBEX (denoted in blue) align closely with libration regions, or resonant islands, in the planar Poincaré map represented in the (ϖ, a) plane. This correlation suggests that planar dynamics can effectively inform spatial dynamics when analyzed within the (ϖ, a) parameter space, a relationship worthy of further study. Additionally, sequential perigee mappings corresponding to the two resonant islands exhibit an approximately conserved area on the (ϖ, a) plane. This behavior reflects the connection between orbital elements and their corresponding Delaunay variables, thus adhering to the integral invariants of Poincaré–Cartan (see Appendix A.3). The mappings from the CR3BP for TESS and IBEX conform closely to expected stability profiles, indicating that TESS is situated near the separatrix of the 2:1 resonance, bordering regions of chaotic dynamics, whereas IBEX occupies a stable inner torus within the 3:1 resonance. The high-fidelity propagated perigee states of TESS and IBEX cluster around the stable islands of the 2:1 and 3:1 resonances, respectively. Discrepancies in the shape of island clusters between high-fidelity states and the PCR3BP stable islands are expected due to the inclusion of the effect of the eccentricity of the Moon and the effect of the sun.

Conversely, the CR3BP propagation of Spektr-R exhibits a trajectory in the unstable region of influence of the 3:1 resonance, that is, within the chaotic resonance zone. In this regime, the trajectory circulates rather than librates, reflecting the absence of stable confinement within a librating island chain. The ephemeris perigee crossings are dispersed similarly, corroborating its navigation within an unstable dynamical regime during the studied period. This analysis reinforces the utility of the CR3BP framework to delineate satellite dynamics and resonance stability, which is validated by high-fidelity propagation analysis, highlighting the Earth–Moon system as an astrodynamics laboratory [45].

IX. Conclusions

Poincaré sections at perigee provide a detailed depiction of the dynamical structure within cislunar space, highlighting both stable islands and chaotic regions, all depicted in geocentric orbital elements which remain immensely useful for cislunar space. This paper's results highlight the pronounced impact of the 2:1 and 3:1 resonances, with a special focus on stable resonance widths and the expansive unstable chaotic resonance zones. The authors' findings highlight the limitations of semi-analytical approaches (i.e., Gallardo's algorithm) in assessing the influence of MMRs in cislunar space. The CR3BP model more accurately captures resonance regions through stable libration widths and chaotic zones. In the Earth–Moon system, PCR3BP widths reveal a structure not seen in small-μ systems (e.g., asteroid or Kuiper belts). Analysis of unstable resonant periodic orbits identifies chaotic regions shaped by manifold interactions. The authors quantify the chaotic zones associated with the 2:1 and 3:1 lunar MMRs and depict them in geocentric orbital elements. By comparing with cataloged xGEO space objects such as TESS, IBEX, and Spektr-R, using TLEs and higher-fidelity ephemeris propagations, they find that their broader resonance regions align more closely with objects known to occupy the 3:1 and 2:1 MMRs than previous approaches. This is especially true for IBEX and TESS, underscoring the Earth–Moon system as a distinct astrodynamics laboratory compared to other celestial systems. Extending these resonance widths and chaotic zones across a wider set of MMRs yields an *atlas* that improves identification of whether space assets reside in stable or unstable orbital regimes. This global dynamics examination of MMRs in the CR3BP sharpens the understanding of the complex behavior of xGEO objects, with direct implications for mission design and cislunar space domain awareness.

Appendix A:

A.1. Continuous Function in ℓ for Perigee Detection

As described in Sec. III.A, we need a continuous real-valued function on the PCR3BP phase space which is zero on Σ_C. Generally a smooth continuous function like $\cos\theta = \boldsymbol{r}\cdot\boldsymbol{v}/(\|\boldsymbol{r}_m\|\|\boldsymbol{v}_m\|)$ is used to detect perigee crossings, where $\boldsymbol{r}$ and $\boldsymbol{v}$ are the Earth-centered inertial frame position and velocity vectors respectively. In the Kepler problem, where $\dot{\ell}$ is always positive, $\cos\theta$ crosses zero in increasing and decreasing directions only at perigee and apogee, respectively. However, in the Earth–Moon system, where μ is large, it was noticed that when the spacecraft comes close to the Moon near apoapse ($\ell = \pi$) the (geocentric) osculating mean anomaly can sometimes actually start *decreasing* in time. In such cases, $\cos\theta$ can pass zero in an increasing direction, mirroring the expected behavior at perigee *despite being at apogee*. Using zero up-crossings of $\cos\theta$ to detect perigee can hence cause false positives. Therefore, we introduce a new continuous real-valued function for event detection during numerical integration:

$$h(\ell) = \cos\ell + \frac{1}{4}\sin\ell - 1 \tag{A1}$$

where $h(\ell)$ only crosses zero in an increasing direction when $\ell = 0$ (perigee) and its other zero only occurs far from apogee and the Moon. This effectively prevents false detections of perigee from occurring at apogee where $\ell = \pi$.

A.2. Transformation from Inertial Ecliptic Frame (ECLIPJ2000) to Nondimensional Synodic Frame

To plot high-fidelity Horizon and Cowell's four-body integration data onto the Poincaré map, a conversion of spacecraft state is required from the inertial geocentric ecliptic frame to the synodic frame under the CR3BP assumptions described in Ref. [46], Sec. III.C.14. For this conversion, the position and velocity vectors of the Moon are also needed. They are obtained in the inertial geocentric equatorial frame using the MATLAB® function `planetEpheme-ris`, and then converted into the ecliptic frame using the rotation matrix,

$$R_{\text{eci}}^{\text{eclip}} = \begin{bmatrix} 1 & 0 & 0 \\ 0 & \cos\varepsilon & \sin\varepsilon \\ 0 & -\sin\varepsilon & \cos\varepsilon \end{bmatrix} \tag{A2}$$

where ε denotes the obliquity of the ecliptic, given by [39] $\varepsilon = (\pi/180)[23 + (26/60) + (21.412/3600)]$ rad.

Denote the position and velocity of the Moon in the inertial geocentric ecliptic frame as $\boldsymbol{r}_m$ and $\boldsymbol{v}_m$. The angular velocity of the Moon, assuming circular motion, is then calculated as

$$\omega_m = \sqrt{\frac{\mathcal{G}(m_e + m_m)}{|\boldsymbol{r}_m|^3}} \tag{A3}$$

The Moon's unit angular momentum vector is given by

$$\hat{\boldsymbol{h}} = \frac{\boldsymbol{r}_m \times \boldsymbol{v}_m}{|\boldsymbol{r}_m \times \boldsymbol{v}_m|} \tag{A4}$$

Hence, the Moon's angular velocity vector becomes $\boldsymbol{\omega}_m = \omega_m\hat{\boldsymbol{h}}$, and the velocity of the Moon under the circular motion assumption becomes

$$\boldsymbol{v}_{m,\text{cir}} = \boldsymbol{\omega}_m \times \boldsymbol{r}_m \tag{A5}$$

The synodic coordinate system moves about the primary (Earth) with the same angular speed as the secondary (the Moon). The instantaneous unit basis vectors $\hat{\boldsymbol{x}}, \hat{\boldsymbol{y}}, \hat{\boldsymbol{z}}$ for the synodic frame can be defined using the position vector of the Moon from the Earth $\boldsymbol{r}_m$ and the velocity vector of the Moon under the circular assumption ($\boldsymbol{v}_m = \boldsymbol{v}_{m,\text{cir}}$) as follows:

$$\hat{\boldsymbol{x}} = \frac{\boldsymbol{r}_m}{|\boldsymbol{r}_m|}, \qquad \hat{\boldsymbol{y}} = \frac{(\boldsymbol{r}_m \times \boldsymbol{v}_m) \times \boldsymbol{r}_m}{|(\boldsymbol{r}_m \times \boldsymbol{v}_m)||\boldsymbol{r}_m|}, \qquad \hat{\boldsymbol{z}} = \frac{\boldsymbol{r}_m \times \boldsymbol{v}_m}{|\boldsymbol{r}_m \times \boldsymbol{v}_m|} \tag{A6}$$

In the absence of external torques (such as perturbations due to other Solar System bodies), the rates of change of the synodic frame unit vectors $\hat{\boldsymbol{x}}, \hat{\boldsymbol{y}}, \hat{\boldsymbol{z}}$ become

$$\dot{\hat{\boldsymbol{x}}} = \frac{\boldsymbol{v}_m}{|\boldsymbol{r}_m|} - \frac{\boldsymbol{r}_m(\boldsymbol{r}_m \cdot \boldsymbol{v}_m)}{|\boldsymbol{r}_m|^3},$$
$$\dot{\hat{\boldsymbol{y}}} = \frac{(\boldsymbol{r}_m \times \boldsymbol{v}_m) \times \boldsymbol{v}_m}{|\boldsymbol{r}_m||\boldsymbol{r}_m \times \boldsymbol{v}_m|} - \frac{(\boldsymbol{r}_m \times \boldsymbol{v}_m)}{|\boldsymbol{r}_m|^3|\boldsymbol{r}_m \times \boldsymbol{v}_m|}((\boldsymbol{r}_m \times \boldsymbol{v}_m) \times \boldsymbol{r}_m),$$
$$\dot{\hat{\boldsymbol{z}}} = 0 \tag{A7}$$

Equations (A6) and (A7) yield $\hat{\boldsymbol{x}}, \hat{\boldsymbol{y}}, \hat{\boldsymbol{z}}, \dot{\hat{\boldsymbol{x}}}, \dot{\hat{\boldsymbol{y}}}, \dot{\hat{\boldsymbol{z}}}$ in geocentric inertial ecliptic coordinates. Thus, the rotation matrix to convert from the geocentric inertial ecliptic frame to the synodic frame is [46]

$$R^{\text{syn}}_{\text{iner}} = \begin{bmatrix} \tilde{Q} & \tilde{0} \\ \dot{\tilde{Q}} & \tilde{Q} \end{bmatrix} \tag{A8}$$

where, interpreting $\hat{\boldsymbol{x}}, \hat{\boldsymbol{y}}, \hat{\boldsymbol{z}}$ as 3×1 column vectors, $\tilde{Q}, \dot{\tilde{Q}}$ are 3×3 matrices given by

$$\tilde{Q} = \begin{bmatrix} \hat{\boldsymbol{x}} & \hat{\boldsymbol{y}} & \hat{\boldsymbol{z}} \end{bmatrix}^T, \qquad \dot{\tilde{Q}} = \begin{bmatrix} \dot{\hat{\boldsymbol{x}}} & \dot{\hat{\boldsymbol{y}}} & \dot{\hat{\boldsymbol{z}}} \end{bmatrix}^T \tag{A9}$$

The position and velocity of the barycenter of the synodic frame can be expressed in the geocentric inertial frame as

$$\boldsymbol{R}_0 = \mu \boldsymbol{r}_m, \qquad \boldsymbol{V}_0 = \mu \boldsymbol{v}_m \tag{A10}$$

where $\mu = m_m/(m_m + m_e)$ is the mass parameter of the Earth–Moon system. The spacecraft state is converted from inertial geocentric ecliptic to synodic coordinates by shifting the origin to the barycenter and transforming $(\boldsymbol{r}, \boldsymbol{v})$ into the rotating synodic frame using Eq. (A8):

$$\begin{bmatrix} \boldsymbol{r}_{\text{syn}} \\ \boldsymbol{v}_{\text{syn}} \end{bmatrix} = R^{\text{syn}}_{\text{iner}} \begin{bmatrix} \boldsymbol{r} - \boldsymbol{R}_0 \\ \boldsymbol{v} - \boldsymbol{V}_0 \end{bmatrix} \tag{A11}$$

Finally, the vectors $\boldsymbol{r}_{\text{syn}}$ and $\boldsymbol{v}_{\text{syn}}$ obtained in Eq. (A11) are nondimensionalized using the magnitude of instantaneous position vector of the Moon. The nondimensional constants are given as

$$l^* = |\boldsymbol{r}_m|, \qquad \mu^* = \mathcal{G}(m_e + m_m), \qquad t^* = \sqrt{\frac{l^{*3}}{\mu^*}} \tag{A12}$$

The nondimensionalized spacecraft state vectors to be used with the CR3BP then become

$$\boldsymbol{r}_{\text{syn,non-dim}} = \frac{\boldsymbol{r}_{\text{syn}}}{l^*}, \qquad \boldsymbol{v}_{\text{syn,non-dim}} = \boldsymbol{v}_{\text{syn}} * \frac{t^*}{l^*} \tag{A13}$$

A.3. Integral Invariants of Poincaré–Cartan

All Hamiltonian systems preserve the Poincaré–Cartan integral invariants under a canonical transformation. That is, a set in $2n$-dimensional phase space can be projected onto n 2D planes formed by a conjugate-coordinate axis system; the oriented sum of the areas of these projections is preserved as the set evolves under Hamiltonian dynamics. Our two-dimensional Poincaré surface of section at perigee is an oriented projection of a four-dimensional Hamiltonian system and follows area preservation, as discussed later. In the planar CR3BP model (four-dimensional phase space) the canonical conjugate-coordinate pairs are (g, G) and (ℓ, L). In this planar case, g represents the same synodic longitude of perigee ϖ defined earlier. Extending to the spatial CR3BP model the phase space becomes six-dimensional, introducing an additional canonical pair (h, H) and redefining g as the (inertial) *argument* of perigee rather than ϖ. These canonical coordinates are called synodic Delaunay variables and are closely related to orbital elements as

$$\begin{aligned} L &= \sqrt{(1-\mu)a}, & \ell &= M, \\ G &= L\sqrt{1-e^2}, & g &= \omega, \\ H &= G\cos i, & h &= \Omega \end{aligned} \tag{A14}$$

where Ω is the synodic longitude of ascending node, that is, the angle between the ascending node direction and the *rotating frame* x axis.

Because we take an oriented surface of section Σ_C at perigee $\ell = 0$, the area of the projection of any subset of Σ_C in the (ℓ, L) plane goes to zero. In the PCR3BP, the entire (invariant) area sum is thus projected onto the (g, G) plane. However, in the spatial CR3BP six-dimensional phase space, the sum of oriented areas projected onto the three canonical coordinate-conjugate pairs [(g, G), (h, H), and (ℓ, L)] remains invariant through sequential mappings at perigee, that is, through all resonant islands.

For resonant objects such as TESS and IBEX, perigee mappings within the spatial CR3BP produce closed librating curves in both the (g, G) and (h, H) planes. With the perigee surface of section condition ($\ell = 0$), the area in the (ℓ, L) plane again becomes zero. Numerical analysis confirms that the sum of the areas enclosed by librating islands in both the (g, G) and (h, H) planes remains constant across all resonant islands. Because $\varpi = g + \Omega$, the sum of the areas enclosed by librating islands in both the (ϖ, G) and (h, H) also remains constant across all resonant islands, as qualitatively seen in Fig. 15. Given the close relationship between Delaunay variables and traditional orbital elements, our simulations further reveal that the summed areas in the (ϖ, a) and (Ω, i) planes also remain approximately constant, an intriguing observation warranting additional research to elucidate the underlying dynamics.

Acknowledgments

B.K. was supported in part by the National Science Foundation under award number DMS-2202994 and in part by the Air Force Office of Scientific Research under award number FA8655-24-1-7012. Part of this research was carried out at the Jet Propulsion Laboratory, California Institute of Technology, under a contract with NASA. This research was also supported by funding from the U.S. Air Force Office of Scientific Research under award number FA9550-24-1-0194. The present form of this manuscript has greatly benefited from the critical comments and valuable suggestions of numerous colleagues. We are especially grateful to Vladislav Sidorenko of the Keldysh Institute of Applied Mathematics and Renu Malhotra of the Lunar and Planetary Laboratory for insightful discussions on the widths of mean-motion resonances in Solar System dynamics. A.J.R. would also like to thank Tabaré Gallardo of the University of the Republic (Uruguay) for his guidance on the use of his semi-analytical method and Di Wu of Embry-Riddle Aeronautical University for his early implementation of Gallardo's codes.

References

[1] Gallardo, T., "Atlas of the Mean Motion Resonances in the Solar System," *Icarus*, Vol. 184, No. 1, 2006, pp. 29–38. https://doi.org/10.1016/j.icarus.2006.04.001

[2] Malhotra, R., and Zhang, N., "On the Divergence of First-Order Resonance Widths at Low Eccentricities," *Monthly Notices of the Royal Astronomical Society*, Vol. 496, No. 3, 2020, pp. 3152–3160. https://doi.org/10.1093/mnras/staa1751

[3] Dutt, P., and Sharma, R. K., "Analysis of Periodic and Quasi-Periodic Orbits in the Earth–Moon System," *Journal of Guidance, Control, and Dynamics*, Vol. 33, No. 3, 2010, pp. 1010–1017. https://doi.org/10.2514/1.46400

[4] Winter, O., and Murray, C., "Resonance and Chaos: I. First-Order Interior Resonances," *Astronomy and Astrophysics*, Vol. 319, No. 1, July 1997, pp. 290–304.

[5] Vaquero, M., and Howell, K. C., "Leveraging Resonant-Orbit Manifolds to Design Transfers Between Libration-Point Orbits," *Journal of Guidance, Control, and Dynamics*, Vol. 37, No. 4, 2014, pp. 1143–1157. https://doi.org/10.2514/1.62230

[6] Binder, A., and Arnas, D., "Reliable and Repeatable Transit Through Cislunar Space Using 2: 1 Resonant Spatial Orbits," *Journal of Guidance, Control, and Dynamics*, Vol. 47, No. 9, 2024, pp. 1973–1979. https://doi.org/10.2514/1.G007800

[7] Bonasera, S., and Bosanac, N., "Computing Natural Transitions Between Tori Near Resonances in the Earth–Moon System," *Journal of Guidance, Control, and Dynamics*, Vol. 46, No. 3, 2023, pp. 443–454. https://doi.org/10.2514/1.G006941

[8] Meiss, J. D., "Symplectic Maps, Variational Principles, and Transport," *Icarus*, Vol. 64, No. 3, 1992, pp. 795–848. https://doi.org/10.1103/RevModPhys.64.795

[9] Koon, W. S., Lo, M. W., Marsden, J. E., and Ross, S. D., "Heteroclinic Connections Between Periodic Orbits and Resonance Transitions in Celestial Mechanics," *Chaos*, Vol. 10, No. 2, 2000, pp. 427–469. https://doi.org/10.1063/1.166509

[10] Ross, S. D., and Scheeres, D. J., "Multiple Gravity Assists, Capture, and Escape in the Restricted Three-Body Problem," *SIAM Journal on Applied Dynamical Systems*, Vol. 6, No. 3, 2007, pp. 576–596. https://doi.org/10.1137/060663374

[11] Naik, S., Lekien, F., and Ross, S. D., "Computational Method for Phase Space Transport with Applications to Lobe Dynamics and Rate of Escape," *Regular and Chaotic Dynamics*, Vol. 22, No. 3, 2017, pp. 272–297. https://doi.org/10.1134/S1560354717030078

[12] Hiraiwa, N., Bando, M., Nisoli, I., and Sato, Y., "Designing Robust Trajectories by Lobe Dynamics in Low-Dimensional Hamiltonian Systems," *Physical Review Research*, Vol. 6, No. 2, 2024, Paper L022046. https://doi.org/10.1103/PhysRevResearch.6.L022046

[13] Poincaré, H., "Sur un théoreme de géométrie," *Rendiconti del Circolo Matematico di Palermo (1884–1940)*. Vol. 33, Dec. 1912, pp. 375–407. https://doi.org/10.1007/BF03015314

[14] Birkhoff, G. D., "Proof of Poincaré's Geometric Theorem," *Transactions of the American Mathematical Society*, Vol. 14, No. 1, 1913, pp. 14–22. https://doi.org/10.2307/1988766

[15] MacKay, R. S., Meiss, J. D., and Percival, I. C., "Transport in Hamiltonian Systems," *Physica D: Nonlinear Phenomena*, Vol. 13, No. 1–2, 1984, pp. 55–81. https://doi.org/10.1016/0167-2789(84)90270-7

[16] Wiggins, S., "On the Geometry of Transport in Phase Space I. Transport in k-Degree-of-Freedom Hamiltonian Systems, $2 \leq k \leq \infty$," *Physica D: Nonlinear Phenomena*, Vol. 44, No. 3, 1990, pp. 471–501. https://doi.org/10.1016/0167-2789(90)90159-M

[17] Gallardo, T., "Strength, Stability and Three Dimensional Structure of Mean-Motion Resonances in the Solar System," *Icarus*, Vol. 317, No. 1, Jan. 2019, pp. 121–134. https://doi.org/10.1016/j.icarus.2018.07.002

[18] Gallardo, T., "Three-Dimensional Structure of Mean-Motion Resonances Beyond Neptune," *Celestial Mechanics and Dynamical Astronomy*, Vol. 132, No. 2, 2020, p. 9. https://doi.org/10.1007/s10569-019-9948-7

[19] Szebehely, V., *Theory of Orbits: The Restricted Problem of Three Bodies*, Academic Press, New York, 1967, pp. 16–18. https://doi.org/10.1016/B978-0-12-395732-0.X5001-6

[20] Llibre, J., Martinez, R., and Simó, C., "Transversality of the Invariant Manifolds Associated to the Lyapunov Family of Periodic Orbits Near L2 in the Restricted Three-Body Problem," *Journal of Differential Equations*, Vol. 58, No. 1, 1985, pp. 104–156. https://doi.org/10.1016/0022-0396(85)90024-5

[21] Dellnitz, M., Junge, O., Koon, W. S., Lekien, F., Lo, M. W., Marsden, J. E., Padberg, K., Preis, R., Ross, S. D., and Thiere, B., "Transport in Dynamical Astronomy and Multibody Problems," *International Journal of Bifurcation and Chaos*, Vol. 15, No. 03, 2005, pp. 699–727. https://doi.org/10.1142/S0218127405012545

[22] Koon, W. S., Lo, M. W., Marsden, J. E., and Ross, S. D., *Dynamical Systems, the Three-Body Problem and Space Mission Design*, Marsden Books, Pasadena, 2022.

[23] Oshima, K., "3D Stable and Weakly Unstable Periodic Orbits Around the Earth Near the Retrograde Co-Orbital Resonance with the Moon," *Astrophysics and Space Science*, Vol. 367, No. 4, 2022, p. 42. https://doi.org/10.1007/s10509-022-04071-4

[24] Meiss, J. D., and Ott, E., "Markov Tree Model of Transport in Area-Preserving Maps," *Physica D: Nonlinear Phenomena*, Vol. 20, Nos. 2–3, 1986, pp. 387–402. https://doi.org/10.1016/0167-2789(86)90041-2

[25] Schroer, C. G., and Ott, E., "Targeting in Hamiltonian Systems that Have Mixed Regular/Chaotic Phase Spaces," *Chaos*, Vol. 7, No. 4, 1997, pp. 512–519. https://doi.org/10.1063/1.166277

[26] Rom-Kedar, V., and Wiggins, S., "Transport in Two-Dimensional Maps," *Archive for Rational Mechanics and Analysis*, Vol. 109, No. 3, 1990, pp. 239–298. https://doi.org/10.1007/BF00375090

[27] Koon, W. S., Marsden, J. E., Ross, S. D., Lo, M. W., and Scheeres, D. J., "Geometric Mechanics and the Dynamics of Asteroid Pairs," *Annals of the New York Academy of Sciences*, Vol. 1017, No. 1, 2004, pp. 11–38. https://doi.org/10.1196/annals.1311.002

[28] Ross, S. D., and Tallapragada, P., "Detecting and Exploiting Chaotic Transport in Mechanical Systems," *Applications of Chaos and Nonlinear Dynamics in Science and Engineering*, edited by S. Banerjee, L. Rondoni, and M. Mitra, Springer, New York, 2012, pp. 155–183. https://doi.org/10.1007/978-3-642-29329-0_7

[29] Werner, M. A., "Multiple Gravity Assists for Low Energy Transport in the Planar Circular Restricted 3-Body Problem," Virginia Tech, Blacksburg, VA, 2022, http://hdl.handle.net/10919/110928.

[30] Dichmann, D. J., Lebois, R., and Carrico, J. P. Jr, "Dynamics of Orbits Near 3: 1 Resonance in the Earth–Moon System," *Journal of the Astronautical Sciences*, Vol. 60, No. 1, 2013, pp. 51–86. https://doi.org/10.1007/s40295-014-0009-x

[31] Ricker, G. R., Winn, J. N., Vanderspek, R., et al., "Transiting Exoplanet Survey Satellite," *Journal of Astronomical Telescopes, Instruments, and Systems*, Vol. 1, No. 1, 2015, Paper 014003 https://doi.org/10.1117/1.JATIS.1.1.014003

[32] Parker, J. S., and Anderson, R. L., *Low-Energy Lunar Trajectory Design, JPL Deep Space Communications and Navigation Series*, Vol. 12, Wiley, Hoboken, NJ, 2014, pp. 68–70.

[33] Howell, K. C., Davis, D. C., and Haapala, A. F., "Application of Periapse Maps for the Design of Trajectories Near the Smaller Primary in Multi-Body Regimes," *Mathematical Problems in Engineering*, Vol. 2012, No. 1, 2012, Paper 351759. https://doi.org/10.1155/2012/351759

[34] Haro, À., Canadell, M., Figueras, J.-L., Luque, A., and Mondelo, J. M., *The Parameterization Method for Invariant Manifolds: From Rigorous Results to Effective Computations, Applied Mathematical Sciences*, Vol. 195, Springer International Publishing, Cham, 2016. https://doi.org/10.1007/978-3-319-29662-3

[35] Kumar, B., "Multi-Shooting Parameterization Methods for Invariant Manifolds and Heteroclinics of 2 DOF Hamiltonian Poincaré Maps, with Applications to Celestial Resonant Dynamics," preprint arXiv: 2509.03655, 2005.

[36] Kumar, B., Anderson, R. L., and de la Llave, R., "High-Order Resonant Orbit Manifold Expansions for Mission Design in the Planar Circular Restricted 3-Body Problem," *Communications in Nonlinear Science and Numerical Simulation*, Vol. 97, 2021, Paper 105691. https://doi.org/10.1016/j.cnsns.2021.105691

[37] Wang, X., and Malhotra, R., "Mean Motion Resonances at High Eccentricities: The 2: 1 and 3: 2 Interior Resonances," *Astronomical Journal*, Vol. 154, No. 1, 2017, p. 20. https://doi.org/10.3847/1538-3881/aa762b

[38] Namouni, F., and Morais, M. H. M., "Resonance Libration and Width at Arbitrary Inclination," *Monthly Notices of the Royal Astronomical Society*, Vol. 493, No. 2, 2020, pp. 2854–2871. https://doi.org/10.1093/mnras/staa348

[39] Simon, J., Bretagnon, P., Chapront, J., Chapront-Touzé, M., Francou, G., and Laskar, J., "Numerical Expressions for Precession Formulae and Mean Elements for the Moon and the Planets," *Astronomy and Astrophysics*, Vol. 282, Feb. 1994, pp. 663–683.

[40] Lan, L., and Malhotra, R., "Neptune's Resonances in the Scattered Disk," *Celestial Mechanics and Dynamical Astronomy*, Vol. 131, No. 8, 2019, pp. 39–26. https://doi.org/10.1007/s10569-019-9917-1

[41] Poincaré, H., *Les Méthodes Nouvelles de la Mécanique Céleste (New Methods in Celestial Mechanics)*, Vols. 1–3, Gauthier-Villars, Paris, 1892–1899, Gauthier-Villars, Paris, New York, 1892-1899; Reprinted by Dover, New York, 1957.

[42] Kumar, B., Rawat, A., Rosengren, A. J., and Ross, S. D., "Cislunar Resonant Transport and Heteroclinic Pathways: From 3:1 to 2:1 to L1,"

Advances in Space Research, 2025.
https://doi.org/10.1016/j.asr.2025.12.005

[43] Amato, D., Bombardelli, C., Baú, G., Morand, V., and Rosengren, A. J., "Non-Averaged Regularized Formulations as an Alternative to Semi-Analytical Orbit Propagation Methods," *Celestial Mechanics and Dynamical Astronomy*, Vol. 131, No. 5, May 2019, p. 21.
https://doi.org/10.1007/s10569-019-9897-1

[44] Shevchenko, I., *The Lidov–Kozai Effect—Applications in Exoplanet Research and Dynamical Astronomy*, Springer, Berlin, 2017.
https://doi.org/10.1007/978-3-319-43522-0

[45] Alessi, E. M., Masdemont, J., and Rossi, A., "The Earth–Moon System as a Dynamical Laboratory," *Frontiers in Astronomy and Space Sciences*, Vol. 6, 2019, p. 43.
https://doi.org/10.3389/fspas.2019.00043

[46] Long, A. C., Cappellari, J. O., Velez, C. E., and Fuchs, A. J., "Goddard Trajectory Determination System (GTDS): Mathematical Theory, Revision 1," NASA TR FDD/552-89/001, 1989.

P. Gurfil
Associate Editor